Monthly Notices
of the
ROYAL ASTRONOMICAL SOCIETY

MNRAS **450,** 128–144 (2015) doi:10.1093/mnras/stv536

The benchmark black hole in NGC 4258: dynamical models from high-resolution two-dimensional stellar kinematics

Daniel Alf Drehmer,[1,2]★ Thaisa Storchi-Bergmann,[1] Fabricio Ferrari,[3] Michele Cappellari[4] and Rogemar A. Riffel[5]

[1]*Instituto de Física, Universidade Federal do Rio Grande do Sul, CP 15051, Porto Alegre 91501-970, RS, Brazil*
[2]*Departamento de Tecnologia, Universidade Estadual de Maringá, 87506-370 Umuarama, PR, Brazil*
[3]*Instituto de Matemática Estatística e Física, Universidade Federal de Rio Grande, CP 474, 96201-900 Rio Grande, RS, Brazil*
[4]*Sub-department of Astrophysics, Department of Physics, University of Oxford, Denys Wilkinson Building, Keble Road, Oxford OX1 3RH, UK*
[5]*Departamento de Física, Centro de Ciências Naturais e Exáątas, Universidade Federal de Santa Maria, 97105-900 Santa Maria, RS, Brazil*

Accepted 2015 March 9. Received 2015 March 5; in original form 2014 August 5

ABSTRACT

NGC 4258 is the galaxy with the most accurate (maser-based) determination for the mass of the supermassive black hole (SMBH) in its nucleus. In this work, we present a two-dimensional mapping of the stellar kinematics in the inner 3.0 arcsec × 3.0 arcsec = 100 pc × 100 pc of NGC 4258 using adaptive-optics observations obtained with the Near-Infrared Integral Field Spectrograph of the Gemini North telescope at an ≈0.11 arcsec (4 pc) angular resolution. The observations resolve the radius of influence of the SMBH, revealing an abrupt increase in the stellar velocity dispersion within ≈10 pc from the nucleus, consistent with the presence of an SMBH there. Assuming that the galaxy nucleus is in a steady state and that the velocity dispersion ellipsoid is aligned with a cylindrical coordinate system, we constructed a Jeans anisotropic dynamical model to fit the observed kinematics distribution. Our dynamical model assumes that the galaxy has axial symmetry and is constructed using the multi-Gaussian expansion method to parametrize the observed surface brightness distribution. The Jeans dynamical model has three free parameters: the mass of the central SMBH ($M_\bullet$), the mass–luminosity ratio (Γ_k = M/L) of the galaxy and the anisotropy of the velocity distribution. We test two types of models: one with constant velocity anisotropy, and another with variable anisotropy. The model that best reproduces the observed kinematics was obtained considering that the galaxy has radially varying anisotropy, being the best-fitting parameters with 3σ significance $M_\bullet = 4.8^{+0.8}_{-0.9} \times 10^7\,\mathrm{M}_\odot$ and $\Gamma_k = 4.1^{+0.4}_{-0.5}$. This value for the mass of the SMBH is just 25 per cent larger than that of the maser determination and 50 per cent larger that a previous stellar dynamical determination obtained via Schwarzschild models for long-slit data that provides an SMBH mass 15 per cent lower than the maser value.

Key words: galaxies: individual: NGC 4258 – galaxies: kinematics and dynamics.

1 INTRODUCTION

NGC 4258 (M 106) is a spiral galaxy with Hubble type SABbc, at a distance of 7.28 ± 0.3 Mpc (Herrnstein et al. 1999), which harbours one of the closest active galactic nucleus (AGN), classified as Seyfert 1.9. This galaxy is well known from previous studies for harbouring the supermassive black hole (SMBH) with the best-constrained mass after that of the Milky Way, with a value of $M_{\bullet\,\mathrm{Maser}} = (3.82 \pm 0.2) \times 10^7\,\mathrm{M}_\odot$, obtained from resolved kinematics of a rotating H_2O maser disc within 0.13 pc from the nucleus (Greenhill et al. 1995; Miyoshi et al. 1995; Herrnstein et al. 1999). It is also well known for its anomalous arms, which resemble spiral arms but are more diffuse than regular spiral arms (Wilson, Yang & Cecil 2001). The anomalous arms span 5 arcmin in optical line emission and 10 arcmin in radio continuum emission (Cecil et al. 2000).

A nuclear non-stellar continuum and broad optical emission lines have been observed in polarized light (Wilkes et al. 1995), supporting the presence of an obscured AGN, from which a radio jet is observed propagating perpendicularly to the maser disc (Cecil, Wilson & Tully 1992). The jet is oriented at a position angle (hereafter PA) PA = −3° ± 1°, consistent with the projected spin axis orientation of the maser disc, which has a major axis PA = 86° ± 2°

★ E-mail: alfdrehmer@gmail.com

(Cecil et al. 2000). Farther from the nucleus, interactions between the radio jet and the interstellar gas are probably the origin of the anomalous arms (Wilson et al. 2001, and references therein).

In the infrared (hereafter IR), the nuclear continuum has been found to be well reproduced by a power-law $f_\nu \propto \nu^{-1.4}$, which seems to extend through the optical to the ultraviolet (Yuan et al. 2002). In X-rays, the nuclear spectrum presents several components: two power laws, a thermal component and the Fe Kα emission line (Yang et al. 2007). The nuclear source is not resolved in the IR (1 to 18 μm spectral region) in observations with 0.2 arcsec angular resolution and presents total luminosity of 2×10^8 $L_\odot$ (Chary et al. 2000).

The host galaxy disc has the photometric major axis at PA = 150°, as obtained from H I observations (van Albada 1980), who have also obtained an inclination for the disc of $i = 72°$. A previous Hα study by van der Kruit (1974) gave values of PA = 146° and $i = 64°$. More recently Sawada-Satoh et al. (2007) have mapped the large scale molecular CO(2–1) velocity field and concluded it is dominated by rotation in a disc with major axis PA = 160° and i = 65.6.

Other studies include the one of Pastorini et al. (2007), who measured the gas kinematics close to the nucleus using long-slit spectra obtained with the Space Telescope Imaging Spectrograph (*HST*-STIS) and that of Herrnstein et al. (2005), who constrained even further the SMBH mass using new maser observations. There is also a more recent study by Siopis et al. (2009) which uses the long-slit spectra from *HST*-STIS to obtain the stellar velocity distribution using the Ca II triplet absorption lines from 2 to 18.2 arcsec along the major axis and to 11.7 arcsec along the minor axis of the galaxy, obtaining a direct determination of the mass of the SMBH.

Adopting the SMBH mass obtained from the kinematics of the maser disc, and using a velocity dispersion for the galaxy bulge of 105 km s^{-1},[1] one can calculate the radius of influence of the SMBH ≈15 pc. For a scale of 35 pc arcsec^{-1}, this radius corresponds to 0.42 arcsec, thus resolvable with ground-based adaptive optics observations, that typically reach 0.1 arcsec in the near-IR. We thus decided to observe NGC 4258 with the Gemini Near-Infrared Integral Field Spectrograph (NIFS) in order to map the stellar kinematics and investigate the effect of the presence of the SMBH in the inner dynamics of the galaxy. Although we also use stellar kinematics to probe the presence of the SMBH as done by Siopis et al. (2009), our *K*-band data are less affected by reddening, allowing the mapping of stellar kinematics much closer to the nucleus than previous observations. In addition, our NIFS data provide a two-dimensional coverage instead of the limited spatial coverage of long-slit observations.

Although the use of dynamical models based on the Schwarzschild orbit superposition method (Schwarzschild 1979) is currently the most popular method to determine the masses of SMBHs in the centre of galaxies, the Jeans dynamical models have proved capable of reproducing the values of the masses of the SMBH in good agreement with those determined by the Schwarzschild models (Krajnović et al. 2009; Cappellari et al. 2010). The Jeans models are also useful when one wants to have more physical insight to the problem. In addition, a Schwarzschild orbit superposition model of NGC 4258 already exists (Siopis et al. 2009), providing a value for the mass of the SMBH of $M_{\bullet\,\mathrm{Schw}} = (3.3 \pm 0.2) \times 10^7$ $M_\odot$, which is comparable to the better constrained value ($M_{\bullet\mathrm{Maser}} = (3.82 \pm 0.02) \times 10^7$ $M_\odot$) derived from maser observations (Herrnstein et al. 2005).

We have thus decided to study the dynamics of the nuclear region of NGC 4258 using our NIFS data and Jeans models in order to determine the dynamical quantities that govern the system. Our goal is also to investigate how well these models reproduce the observed stellar kinematics and how large are the differences between the values of the mass of the SMBH of NGC 4258 determined by different methods. The use of the Jeans anisotropic dynamical model has allowed us to understand how variations in the model parameters – such as the velocity anisotropy and the mass-to-light ratio – affect the stellar kinematics and the determination of the mass of the SMBH in NGC 4258.

This paper is organized as follows. In Section 2, we present our Integral Field Unit (IFU) observations and the photometric data used to construct the dynamical model. In Section 3, we discuss the derivation of the two-dimensional line-of-sight velocity distribution (LOSVD). Section 4 is dedicated to the description of the dynamical model and the discussion of the results and in Section 5 we present our concluding remarks.

2 OBSERVATIONS AND DATA REDUCTION

The Integral Field spectroscopic data were obtained in the near-IR *K*-band with the instrument NIFS (McGregor et al. 2003) operating with the ALTtitude conjugate Adaptive optics for the InfraRed (ALTAIR) adaptive optics module at the 8-m Gemini North telescope in 2007 April under the science programme GN-2007A-Q-25. The *K* band was selected for this study because it contains the absorption CO bands at ≈2.3 μm which can be used to derive the stellar kinematics. In order to obtain the surface brightness distribution to model the galaxy mass density distribution (and the gravitational potential), we used two sets of archive images: the first of them obtained with the Near-Infrared Camera and Multi-Object Spectrometer (NICMOS) NIC2 camera of the *Hubble Space Telescope* (*HST*). The second is a large-scale image from the Two Micron All Sky Survey (2MASS). In the next sections, we describe these sets of data and the reduction procedures.

2.1 The photometric data

2.1.1 NICMOS

Near-IR *K*-band images were obtained from the Multimission Archive at STScI corresponding to data sets N46801050 for object observations and N46801060 for sky observations, from the proposal ID 7230 (Scoville 1997). These observations were obtained with the NIC2 camera of NICMOS using the *F*222*M* filter. The NIC2 camera has 256 pixels × 256 pixels, with scales of 0.075 arcsec pix^{-1} in x and y, providing a field of view of ∼19.2 × 19.2 arcsec^2. The *F*222*M* filter covers the wavelength range 2.15–2.28 μm, with central wavelength at 2.2174 μm. The galaxy observation have a total exposure time of 224 s performed in MULTIACCUM mode with a four-point spiral dither; the sky observations were obtained with a three-point spiral dither.

The data reduction was done with standard IRAF[2] and PYRAF tasks following the same steps as in Chary et. al. (2000). We used the

[1] This is the average value of the velocity dispersion in the whole NIFS field of view and not the luminosity-weighted velocity dispersion inside a single aperture that contains the whole galaxy bulge (see Section 3).

[2] IRAF is distributed by the National Optical Astronomy Observatories, which are operated by the Association of Universities for Research in Astronomy, Inc., under cooperative agreement with the National Science Foundation.

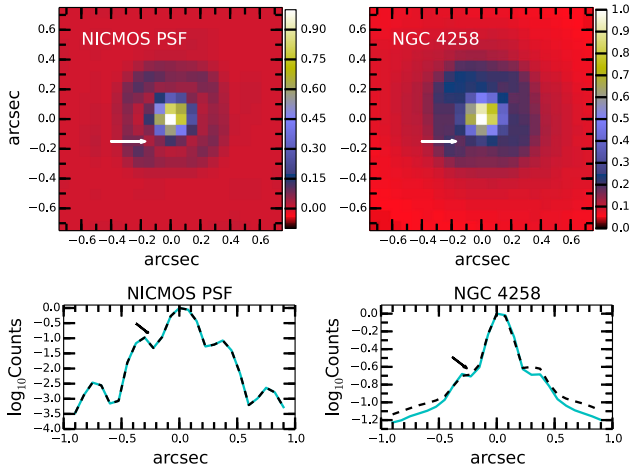

Figure 1. Top left: the NICMOS PSF modelled with the TINYTIM software. Top right: the central 1.5 arcsec of the NICMOS image of the galaxy presenting the features of the NICMOS PSF. Intensity units are normalized counts. The bottom panels show cuts along the two diagonals (dashed line and cyan continuum line) across the upper panels, in logarithmic scale.

MULTIDRIZZLE task to combine the dithered images following the standard sequence for NICMOS dithered observations described in the MULTIDRIZZLE handbook. Inspecting the data quality files, we noted that due the emission of the AGN, some of the pixels at the centre of the galaxy are incorrectly identified as cosmic rays in the four dithered images. We thus corrected this in the data quality files and created a static mask to correct for a spurious 'bar' feature in the column 128. Then a separated drizzled image was created for each dither position of the detector. To determine the need for extra offsets, we have done cross-correlation measurements between the images with the CROSSDRIZ task and the extra shifts have them been computed with the SHIFTFIND task. Then, we ran again the MULTIDRIZZLE with the extra shifts and created new separately drizzled images as well as a well-aligned median image. Finally, we ran MULTIDRIZZLE again to derive the cosmic ray masks and combine the images in a final drizzled image, clean of cosmic rays and detector artefacts.

The compact nuclear emission due to the AGN is evident in the reduced image. This unresolved emission appears in the image as a point source introducing the spurious features of the NICMOS point spread function (PSF) in the image. In the top-left panel of Fig. 1, we show the NICMOS PSF, and in the right-hand panel the central 1.5 arcsec of the image of NGC 4258. In the bottom panels of this figure, we display cuts along the two diagonals of each of the images in the top panels (black dashed and cyan continuous lines). The arrows indicate the strong signature of the PSF in the image of the galaxy. As our interest is to determine the luminosity distribution and gravitational potential generated by the stars, we need to subtract the contribution from the AGN. In order to do this, we generated a large image of the NICMOS PSF and centred it at the same position of the galaxy centre in the detector. We then normalized the PSF image so that its peak flux coincided with that of the galaxy. After several tests in which we multiplied the normalized PSF by different fractions and subtracted it from the galaxy image, we concluded that the smoothest residual (without an 'inverted peak' due to over-subtraction) was obtained with a contribution of the PSF of 70 per cent to the peak of the brightness distribution. The resulting image after reduction and AGN subtraction is shown in the bottom panel of Fig. 2. The rectangle in the centre of the

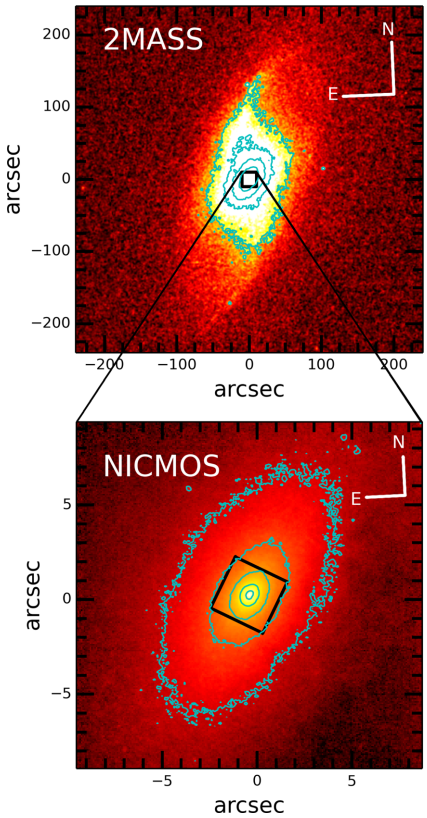

Figure 2. Top: the 2MASS *Ks*-band image. Bottom: the *K*-band image from NICMOS. The rectangle in the bottom panel shows the field of view of our NIFS observations presented in Fig. 3.

image represents the field of view of the NIFS observations. The total amount of light subtracted corresponds to $\approx 1.9 \times 10^7\,L_{\odot K}$. In Appendix C, we perform some tests to evaluate the effects of a possible over- or undersubtraction of the AGN on the determination of the mass of the SMBH.

2.1.2 2MASS

In order to characterize the surface brightness distribution of the galaxy beyond the inner $19.0 \times 19.0\,\mathrm{arcsec}^2$, we used a large-scale image from the 2MASS telescope in the *K*-short-band (*Ks*-band) from Jarrett et al. (2003). The 2MASS image has a scale of 1.0 arcsec pix^{-1} and the *Ks*-filter covers the wavelength range from 1.93 to 2.38 μm with central wavelength of 2.17 μm. The central $8.3 \times 8.3\,\mathrm{arcmin}^2$ of this image is shown in the top panel of Fig. 2. The black rectangle in the centre of the panel represents the field of view of the NICMOS image.

2.2 The NIFS data

NIFS has a square field of view of $\approx 3.0 \times 3.0\,\mathrm{arcsec}^2$, divided into 29 slices with an angular sampling of 0.1 arcsec in *x* and 0.04 arcsec in *y*. The observing procedures followed the standard Object-Sky-Object-Sky-Object-Sky-Object dither sequence, with off-source sky positions since the target is extended, and individual exposure times of 600 s centred at $\lambda = 2.2$ μm with a total of 10 individual exposures at the galaxy. The IFU was oriented with the slices along the position angle PA = 145°. We have used the K_G5605 grating and

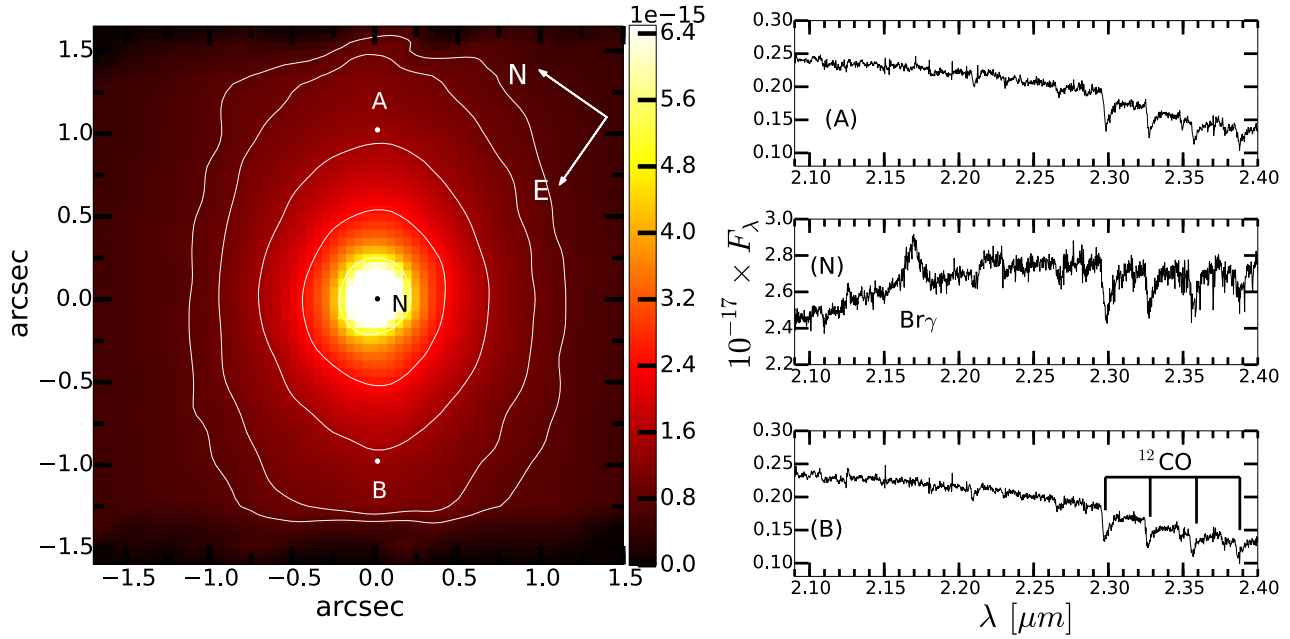

Figure 3. Left: continuum map (reconstructed image) from our NIFS spectroscopy. Right: spectra at the positions A, N and B marked at the left-hand panel with the Brγ emission line and CO absorption bands identified. Flux units are erg s^{-1} cm^{-2} and the extraction apertures are 0.05 arcsec × 0.05 arcsec.

the filter *HK_G*0603, which resulted in an arc lamp line full width at half-maximum (FWHM) of 3.2 Å (thus $R \sim 5300$).

The data reduction was accomplished using tasks contained in the NIFS package which is part of GEMINI IRAF package as well as generic IRAF tasks. The reduction procedure included trimming of the images, flat-fielding, sky subtraction, wavelength and s-distortion calibrations. We have also removed the telluric bands and flux calibrated the frames by interpolating a blackbody function to the spectrum of the telluric standard star. Small shifts between exposures due to guiding problems were corrected by mosaicking the individual data cubes into a final one. The final data cube contains ∼4300 spectra, each corresponding to an angular coverage of 0.5 × 0.5 arcsec^2, which translates into 1.75 × 1.75 pc^2 at the galaxy. The NIFS angular resolution with ALTAIR in the *K*-band is 0.11 arcsec as measured from the FWHM of the spatial profile of the telluric standard stars.

In the left-hand panel of Fig. 3, we present a reconstructed image obtained from the data cube collapsing the spectra in the same wavelength range of the NICMOS *F*222*M* filter, i.e. from 2.15 to 2.28 μm. The right-hand panel of the figure presents three characteristic spectra extracted from the data cube: the nuclear spectrum (position N in the continuum map), a spectrum from a location at 1 arcsec NW of the nucleus (position A) and another from 1 arcsec SE of the nucleus (position B). The only emission line present in the nuclear spectrum is the broad Brγ at 2.1661 μm. The CO absorption bands used to obtain the stellar kinematics are identified in the spectrum from position B.

3 LINE-OF-SIGHT VELOCITY DISTRIBUTION

In order to obtain the LOSVD, we have used the penalized Pixel-Fitting (pPXF) method[3] of Cappellari & Emsellem (2004) to fit the stellar absorptions bands present in the *K*-band spectra. The algorithm finds the best fit to a galaxy spectrum by convolving template stellar spectra with the corresponding LOSVD. This procedure gives as output the radial velocity *V*, velocity dispersion σ and higher order Gauss–Hermite moments h_3 and h_4. The pPXF method allows the use of several template stellar spectra and to vary the weights of the contribution of the different templates to obtain the best fit, minimizing the template mismatch problem. We use the templates from the spectroscopic library of late spectral type stars[4] observed with the Gemini Near Infrared Spectrograph (Winge, Riffel & Storchi-Bergmann 2009), which have an almost identical spectral resolution to that of our data. We have used 60 templates in the pPXF fits, and for all spaxels of the Monte Carlo simulations. We have also restricted the fit to the interval shown in Fig. 4, as for smaller wavelengths there are no features to constrain the stellar kinematics and there may be some contamination from emission lines.

In Fig. 4, we present the resulting pPXF fits to the galaxy spectra from the positions A (top panel), N (middle panel) and B (bottom panel) indicated in Fig. 3. The cyan lines are the galaxy spectra, the black lines are the pPXF fits to the galaxy spectra and the red lines are the residuals. The high signal-to-noise ratio of the IFU data, in the range of 30 to 130 with an average signal-to-noise ratio of ∼50, allows us to obtain fits of very high quality to the observed galaxy spectra without the need for spatial binning. The resulting kinematic maps of the velocity distribution are presented in Fig. 5. The top-left panel shows the velocity field after subtraction of the galaxy systemic velocity of 453 km s^{-1}, determined as the stellar velocity at the location of the peak of the continuum. The centroid velocity field presents a maximum of ∼80 km s^{-1} and a rotation pattern with the line of nodes oriented along the position angle PA = 145° and with the SE side approaching and the NW side receding. The top-right panel shows the map of the stellar velocity dispersion, varying in the range 80–180 km s^{-1}, with a maximum at the location of the peak of

[3] Available from http://purl.org/cappellari/software

[4] Available from: http://www.gemini.edu/sciops/instruments/nearir-resources/?q = node/ 10167

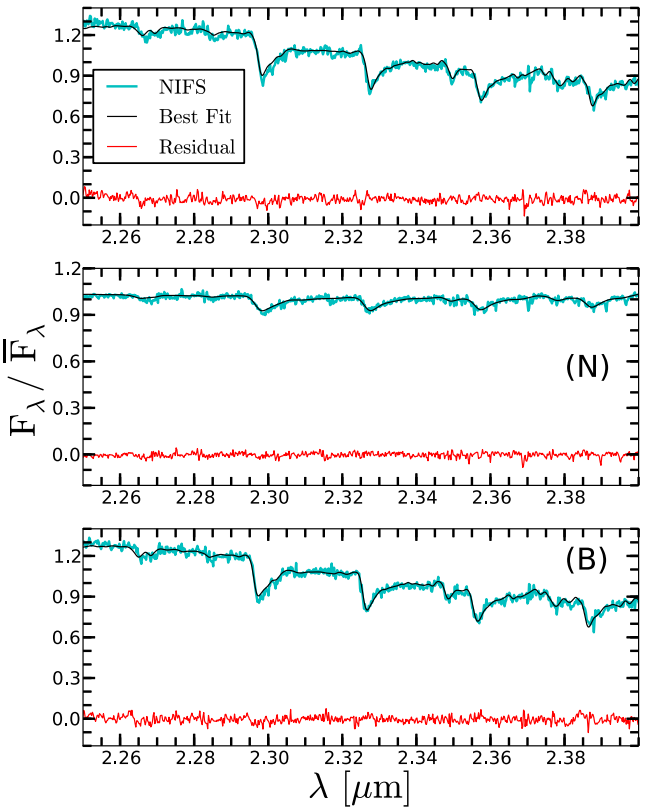

Figure 4. pPXF fits to the galaxy spectra. Examples of the resulting fit of the pPXf to the galaxy spectra on the positions A (top panel), N (middle panel) and B (bottom panel) indicated in Fig. 3; the cyan lines are the galaxy spectra, the black lines are the resulting fits of pPXF to the galaxy spectra and the red lines are the residuals.

the continuum. The average velocity dispersion over the whole field of view is ∼105 km s^{-1}. In Appendix B, we make a comparison of the resulting kinematics with that presented in the paper of Siopis et al. (2009), obtained with the *HST*/STIS instrument. As pointed out in the Introduction, the radius of influence of the SMBH in NGC4258 is $R_{\rm inf} \approx 15$ pc, that corresponds to 0.42 arcsec at the galaxy distance. Fig. 5 shows that inside this radius there is indeed a sharp rise in the σ values as expected for the region where the SMBH dominates the gravitational potential, what is probably better seen in Fig. 6. The lower panels show the Gauss–Hermite h_3 and h_4 moments with values ranging from −0.15 to 0.15.

The errors in the centroid velocities and velocity dispersions were calculated from 850 Monte Carlo simulations and are illustrated in Fig. 6. The left-hand panel of this figure presents the values of the measured centroid velocity (V) obtained from a cut along the galaxy major axis (black points) and the 1σ error bar from the Monte Carlo simulation (shaded band). The average standard deviation of the velocities is 3.3 km s^{-1}, with a maximum of 8.4 km s^{-1} in the central pixel. Ignoring the region around the galaxy minor axis, where the velocities are approximately zero, the average velocity error is lower than 10 per cent. The right-hand panel shows de values of the measured velocity dispersions (σ) (black points) and the 1σ error bar (shaded band) along the galaxy major axis. The average standard deviation in the velocity dispersion is 4.1 km s^{-1}, with a maximum of 10.2 per cent in the central pixel, an average error corresponding to 4 per cent. The errors in the central region of the data cube are higher than at the edges because of the presence of absorption features stronger in the nucleus than outside, that we attribute to the effect of dust and dilution by a red continuum from the AGN dusty torus.

4 DYNAMICAL MODELLING

4.1 Surface brightness distribution

In order to model the galaxy surface brightness distribution we use the MGE_FIT_SECTORS package[5] (Cappellari 2002) which performs a Multi-Gaussian Expansion (MGE) parametrization for the observed surface brightness of the galaxy (Emsellem, Monnet & Bacon 1994). In what follows, we present the most relevant steps in applying the MGE model to the galaxy NGC 4258 (see Cappellari (2008) for a complete description of the method).

The surface brightness distribution in the plane of the sky can be described by the sum of a set of two-dimensional concentric Gaussians as

$$\Sigma(x', y') = \sum_{k=1}^{N} \frac{L_k}{2\pi\sigma'^2_k q'_k} \mathrm{e}^{\left[-\frac{1}{2\sigma'^2_k}\left(x'^2 + \frac{y'^2}{q'^2_k}\right)\right]}, \quad (1)$$

where N is the number of the Gaussians, each with total luminosity L_k, axial ratio between $0 \leq q'_k \leq 1$ and dispersion σ'_k along the major axis ($x\prime$). In this reference system, the $x\prime$ axis is aligned with the galaxy photometric major axis, derived from the photometry of the 2MASS image, which is oriented at PA = 156°, and $z\prime$ points to the line of sight. Before comparing equation (1) with the observed surface brightness distribution, it is convolved with an MGE model for the NICMOS PSF. The NICMOS PSF was obtained with the TINYTIM software (Krist, Hook & Stoehr 2010). The MGE parameters of the modelled NICMOS PSF are presented in Table A1 of Appendix A. In Fig. A1, we present a comparison of the MGE model and the TINYTIM PSF. To examine how important are the effects of the small differences between the MGE model and the TINYTIM PSF in the convolution procedure, we present in Fig. A2 a comparison between the surface brightness distribution convolved with the TINYTIM PSF and the one convolved with the MGE model for the PSF. Fortunately, the two convolved surface brightness distributions are very similar. This comparison show that the two are practically indistinguishable.

In order to reproduce the surface brightness distribution of NGC 4258, we fit together the 2MASS and NICMOS K-band images using the MGE_FIT_SECTORS package. NGC 4258 has an angular size of 18.6 × 7.2 arcmin^2. The NICMOS image has an angular size of ∼19.2 × 19.2 arcsec^2 and is used to fit the surface brightness distribution in the central region of the galaxy. Due to the large 2MASS PSF, we do not use the 2MASS image in the fit of the nuclear region ($R \leq 6.0$ arcsec). From the radius 6.0 arcsec to the edges of the galaxy, we fit the two images (NICMOS and 2MASS) together. As NGC 4258 is a spiral galaxy with a small bulge and a large disc component, we implemented a two-component MGE parametrization by separating the Gaussians in two sets with different constraints for the axial ratios (q'_k). The first with $0.45 \leq q'_k \leq 0.46$ to model the disc component, and the second set with more flexible constraints, $0.5 \leq q'_k \leq 0.99$, to model the other galaxy components.

After several attempts, we obtained a satisfying fit of the galaxy surface brightness distribution using a set of 12 Gaussians centred in the galaxy nucleus and with the major axis aligned with the galaxy photometric major axis. In Table 1, we present the parameters

[5] Available from: http://purl.org/cappellari/software

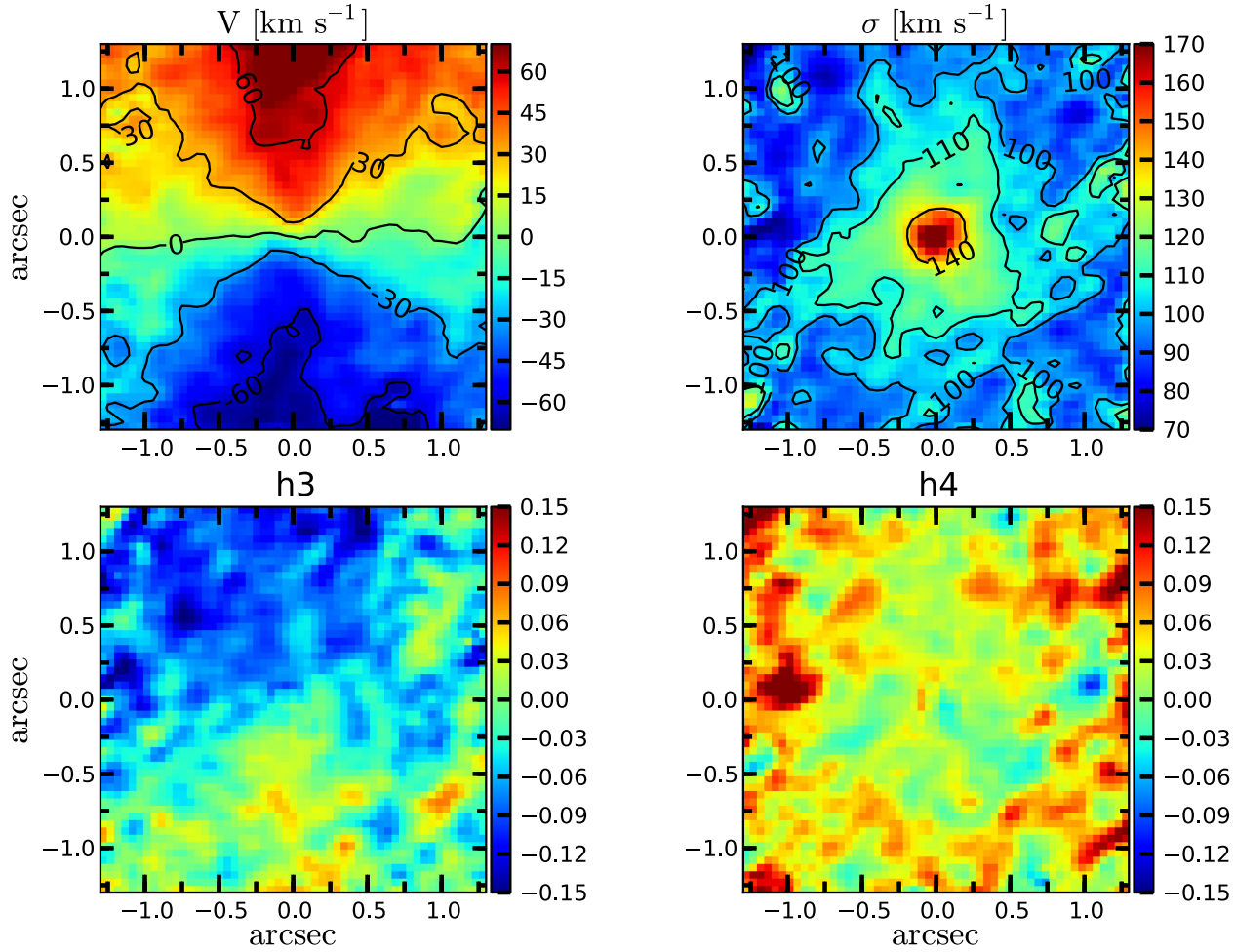

Figure 5. Two-dimensional stellar kinematic maps of NGC 4258. Top left: centroid velocity field. Top right: velocity dispersion. Bottom: Gauss–Hermite moments h_3 (left) and h_4 (right). Orientation as in Fig. 3 where the negative y-axis is at 145° relative to the north direction.

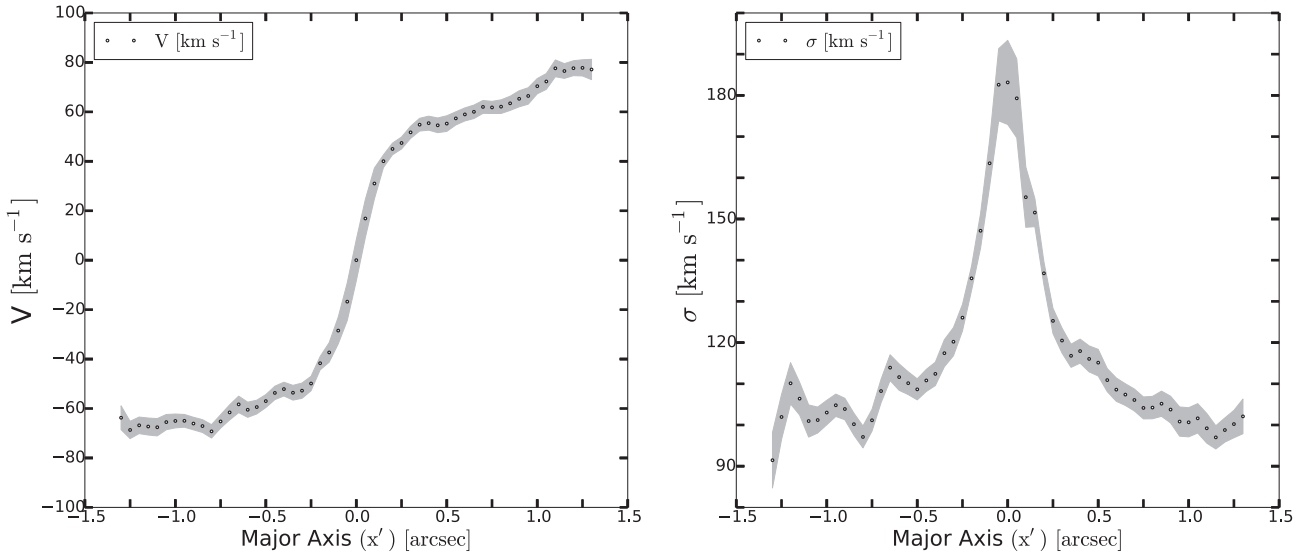

Figure 6. Measured values and Monte Carlo error estimation for the velocities and velocity dispersions along the galaxy major axis. Left: measured values of the velocities V with the 1σ error bar obtained from 850 Monte Carlo simulations. Right: measured values of the velocity dispersions with the 1σ error bar.

Table 1. Gaussian parameters of the MGE model.

I'_k ($L_\odot$ pc^{-2})	σ'_k (arcsec)	q'_k
247 712.8	0.063	0.693
28 902.5	0.280	0.926
9432.3	0.501	0.460
10 244.6	0.981	0.655
3726.7	2.677	0.460
2193.7	3.525	0.583
607.5	6.336	0.460
627.3	9.022	0.698
387.3	18.700	0.658
126.7	41.920	0.756
181.2	93.476	0.450
16.9	247.722	0.500

Note: the first column lists the surface brightnesses of each Gaussian in units $L_\odot$ pc^{-2}; the second column lists the Gaussian dispersions along the major axis in arcseconds; the third column lists the axial ratios of the Gaussians.

of the Gaussians of our best fit: the first column lists the surface brightnesses ($I'_k = \frac{L_k}{2\pi\sigma_k'^2 q'_k}$) in units of $L_\odot$ pc^{-2}, the second column lists the Gaussian dispersions σ'_k in arcseconds and the third column lists the axial ratios q'_k. In Fig. 7, we present linear cuts across the galaxy centre: along the galaxy photometric major axis in the left-hand panel and along the photometric minor axis in the right-hand panel. The cyan continuous lines correspond to the MGE surface brightness distribution, the black open circles correspond to the observed brightness distribution in the NICMOS image and the red points correspond to the MGE after convolution with the NICMOS PSF ($\Sigma \otimes$PSF). In both panels, the modelled convolved surface brightness distribution provides a good reproduction of the observed one for the inner 6 arcsec of the galaxy that is approximately two times the size of the region where we have kinematic measurements. Due the presence of the spiral arms and of isophotal twist, the surface brightness distribution in the outer region of the galaxy cannot be well reproduced by the MGE model. The good agreement of the red points with the open circles shows the good quality of the MGE model in describing the galaxy surface brightness distribution.

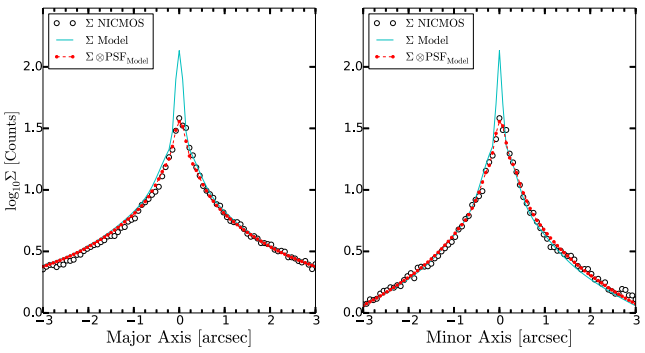

Figure 7. MGE model for the central 6.0 × 6.0 arcsec^2 of NGC 4258 compared to the NICMOS image. Left: cuts along galaxy major axis of the modelled surface brightness distribution (blue line), observed surface brightness distribution (black open circles) and the modelled convolved surface brightness distribution (red points). Right: same as in the left for the galaxy minor axis.

4.1.1 Mass density and gravitational potential

In order to obtain the deprojected three-dimensional luminosity density, we adopt the approximation that the galaxy is axisymmetric. In this case, the luminosity density can be obtained from the parameters that describe the projected surface luminosity density. Assuming that the galaxy is oblate-axisymmetric, the luminosity density can be obtained from

$$\nu(R,z) = \sum_{k=1}^{N} \frac{L_k}{\left(\sqrt{2\pi}\sigma_k\right)^3 q_k} \mathrm{e}^{\left[-\frac{1}{2\sigma_k^2}\left(R^2+\frac{z^2}{q_k^2}\right)\right]}, \quad (2)$$

where, $q_k = \frac{\sqrt{q_k'^2 - \cos^2 i}}{\sin i}$, and i is the galaxy inclination ($i = 90^\circ$ being *edge-on*). It is important to make clear that this approach cannot solve the intrinsic degeneracy of the deprojection.

The galaxy mass density can be described by a set of Gaussians as

$$\rho(R,z) = \sum_{j=1}^{M} \frac{M_j}{\left(\sqrt{2\pi}\sigma_j\right)^3 q_j} \mathrm{e}^{\left[-\frac{1}{2\sigma_j^2}\left(R^2+\frac{z^2}{q_j^2}\right)\right]}. \quad (3)$$

In the self-consistent case, i.e. if only stars contribute, we can obtain the galaxy mass density by the multiplication of the luminous density by a dynamical mass-to-light ratio. In this case, the Gaussians in equation (3) are the same as in equation (2) with $M_j = \Gamma_k L_k$. The gravitational potential generated by this density can be obtained through the Poison equation, $\nabla^2\Phi = 4\pi G\rho$.

The contribution of the SMBH to the gravitational potential is modelled by the approximation that the corresponding distribution of matter is given by an extremely narrow spherical Gaussian. The dispersion of the Gaussian is constrained by the resolution of the kinematic data, such that $3\sigma_\bullet \leq R_{\rm min}$, where $R_{\rm min}$ is the smallest distance from the black hole (BH) that one needs to model.

4.2 The Jeans anisotropic dynamical model

A complete description of the derivation of the Jeans equations (Jeans 1922), can be found in the book of Binney & Tremaine (2008). Here, we only provide an overview of some fundamental assumptions of the model. The model assumes that the galaxy is a large system of stars with positions (x) and velocities (υ) described by a distribution function (DF). If this system is in a steady state under the influence of a smooth gravitational potential, the DF must satisfy the steady-state collisionless Boltzmann equation. Under the assumption that the galaxy has axial symmetry, we obtain the axisymmetric Jeans equations in cylindrical coordinates (Binney & Tremaine 2008, equations 4–29). The solutions of these equations provide the velocity moments of the DF and can be compared with the observed kinematics of the galaxy.

Semi-isotropic Jeans dynamical models (Jeans 1922) of galaxies have been applied for different purposes (Nagai & Miyamoto 1976; Satoh 1980; Binney, Davies & Illingworth 1990; van der Marel, Binney & Davies 1990; Emsellem et al. 1994; van Albada, Bertin & Stiavelli 1995; Riciputi et al. 2005). Two of the most interesting applications are to estimate the dynamical mass-to-light ratio of galaxies (van der Marel 1991; Statler, Dejonghe & Smecker-Hane 1999; Cappellari et al. 2006; Cortés, Kenney & Hardy 2008) and to obtain the masses of the SMBH in the nuclei of galaxies (Magorrian et al. 1998; van der Marel et al. 1998; Cretton & van den Bosch 1999; Joseph et al. 2001).

Cappellari (2008) has presented an anisotropic generalization of the axisymmetric semi-isotropic Jeans formalism. Making the assumption that the velocity ellipsoid is aligned with a cylindrical coordinate system (R, z, ϕ) and that the anisotropy is constant and quantified by $\overline{v_R^2} = b\,\overline{v_z^2}$, the Jeans equations reduce to (equations 8 and 9 of Cappellari 2008)

$$\frac{b\,\nu\overline{v_z^2} - \nu\overline{v_\phi^2}}{R} + \frac{\partial(b\,\nu\overline{v_z^2})}{\partial R} = -\nu\frac{\partial\Phi}{\partial R} \tag{4}$$

$$\frac{(\nu\overline{v_z^2})}{\partial z} = -\nu\frac{\partial\Phi}{\partial z}. \tag{5}$$

One advantage of this approach is that, if an MGE model for the galaxy surface brightness is available, the solutions of the Jeans equations, (i.e. the first and second moments in velocity of the DF of the system, and the projections of these moments in the plane of the sky) are given as a function of the Gaussian parameters of the luminosity density (equation 2) and mass density (equation 3). Cappellari (2008) applied this method to determine the mass-to-light ratio and inclination of galaxies classified as fast-rotators in the SAURON survey (de Zeeuw et al. 2002). The effectiveness of this Jeans Anisotropic MGE dynamical model (JAM)[6] is shown in Cappellari et al. (2009) where they model the observed kinematics of Centaurus A with the same parameters (M/L, $M_\bullet$) obtained from the Schwarzschild orbit superposition method. Another test of the JAM models is presented by Lablanche et al. (2012) where the authors demonstrate the ability of the models in reproducing the anisotropy profile and mass-to-light ratios of realistic *N*-body collisionless simulations of barred and unbarred galaxies. In Medling et al. (2011), the JAM models are used to determine the mass of the SMBH in the southern component of the pair of interacting galaxies in NGC 6240. In Neumayer & Walcher (2012), they established upper limits for the BH masses of nine late-type galaxies using the JAM models. Raimundo et al. (2013) uses the JAM models to obtain an upper limit of the BH mass in MCG-6-30-15. Emsellem (2013) used the JAM models together with *N*-body simulations to review the hypothesis of the presence of an overmassive BH in NGC 1277. Another frequent application of the JAM models is the determination of intermediate-mass BHs in globular clusters (Seth et al. 2010; Lützgendorf et al. 2011, 2012, 2013; Feldmeier et al. 2013). The largest applications of the JAM method to date are the studies of the stellar initial mass function (Cappellari et al. 2012) and dynamical scaling relations (Cappellari et al. 2013b) of the 260 early-type galaxies of the ATLAS^{3D} survey.

The anisotropic Jeans method used in this work is significantly different from Schwarzschild method. The former describes the orbital distribution via a few anisotropy parameters, while the latter makes virtually no assumptions on the orbital distribution. A drawback of the Jeans approach is that it can potentially bias the BH mass determination. However, this issue is largely overcome by allowing for a variation in the anisotropy, which can be constrained by integral-field kinematics, as we do here. Previous tests agree with the result of this paper, showing a general consistency between the Schwarzschild and JAM approach (Cappellari et al. 2010; Seth et al. 2014). An advantage of the Jeans approach is its good predictive power: it is unable to fit the noise of the systematics in the data and can often be used to detect problems with the data or flag bad data (e.g. Cappellari et al. 2013a). The Jeans solutions are also relatively easy to qualitatively understand. The Schwarzschild approach, given its generality in the adopted orbital distribution, does not suffer from potential bias in the BH mass. However, the method can easily fit noise and bad data without raising any concern. The method can easily create unphysical orbital distributions outside the region constrained by the kinematics (e.g. fig. 2 of Cappellari & McDermid 2005). For this reason, it provides better constraints to the SMBH masses when integral-field data are available out to larger radii (Verolme et al. 2002). Overall, the two methods are complementary and sufficiently different to motivate the re-determination of BH mass presented in this paper, using Jean rather than the previously published Schwarzschild approach.

[6] Available from: http://purl.org/cappellari/software

4.2.1 *The velocity second moment*

For a galaxy with a surface brightness distribution parametrized by an MGE model as in Section 4.1, the projection in the plane of the sky of the second moment, $\langle v_{\rm los}^2(x', y')\rangle$ of the DF is given in terms of the parameters of the Gaussians (equation 28 of Cappellari 2008). This quantity is a function of three free parameters: the galaxy mass-to-light ratio (Γ_K), the anisotropy ($\beta_z = 1 - \frac{\overline{v_z^2}}{\overline{v_R^2}}$) and the mass of the SMBH ($M_\bullet$). The comparison of the modelled $\langle v_{\rm los}^2\rangle^{1/2}$ with the measured $V_{\rm rms} = \sqrt{V^2 + \sigma^2}$, where V and σ are shown in Fig. 5, provide the values of the best-fitting parameters for the galaxy.

We start by assuming that the galaxy has a constant anisotropy in the velocity dispersions. Thus the space of parameters has three dimensions: $M_\bullet \times \Gamma_K \times \beta_z$. We then perform a χ^2 minimization in this space searching for the values of $M_\bullet, \Gamma_K$ and β_z that best fit the observed kinematics. We weight the χ^2 minimization by assigning errors to the kinematic measurements that are inversely proportional to the galaxy surface brightness at each location. This is done in an attempt to give comparable contributions to the χ^2 for all radii sampled by the NIFS kinematics. Without this weighting, the χ^2 would be artificially dominated by the numerous pixels at large radii, which contain virtually no information on the mass of the central SMBH. In our trials without weighting the kinematics in the minimization, we have obtained a significantly larger value for the mass of the SMBH ($M_\bullet = 7.2 \times 10^7\,{\rm M}_\odot$), but the modelled values of the velocity second moment clearly did not reproduce the values of the observed $V_{\rm rms}$ for the central region of the galaxy.

We considered in a first trial that the galaxy has an inclination of $i = 72^\circ$ (Model A). This inclination is obtained considering that the outer disc of the galaxy ($r = 200$ arcsec) is thin (van Albada 1980; Siopis et al. 2009). The best-fitting model for this inclination with $\chi^2_{\rm min} = 27.21$ is obtained with the parameters $M_\bullet = 5.2 \times 10^7\,{\rm M}_\odot$, $\Gamma_K = 4.3$ and $b = 0.90\,(\beta_z = -0.11)$. This model does not reproduce satisfactorily the measured kinematics along the galaxy minor axis.

After several attempts with different values for the galaxy inclination, we obtained a satisfactory model for $i = 64^\circ$ (Model C). The minimum χ^2 obtained was $\chi^2_{\rm min} = 25.48$ for $M_\bullet = 4.7 \times 10^7\,{\rm M}_\odot$, $\Gamma_K = 4.1$ and $b = 1.1\,(\beta_z = 0.09)$. In Fig. 8, we show the χ^2 minimization in the space of parameters. In Table 2, we list the best-fitting parameters for three models with different inclinations: the models A and C described before and a third model with an inclination of $i = 68^\circ$ for which the best-fitting parameters are $M_\bullet = 5.0 \times 10^7\,{\rm M}_\odot$, $\Gamma_K = 4.3$ and $b = 0.95\,(\beta_z = -0.05)$, that provide a minimum χ^2 of 26.84. Systematic variations in the best-fitting parameters are observed as the galaxy inclination decreases: the values of the mass of the SMBH and the mass-to-light ratio decrease but the value of the anisotropy parameters increase.

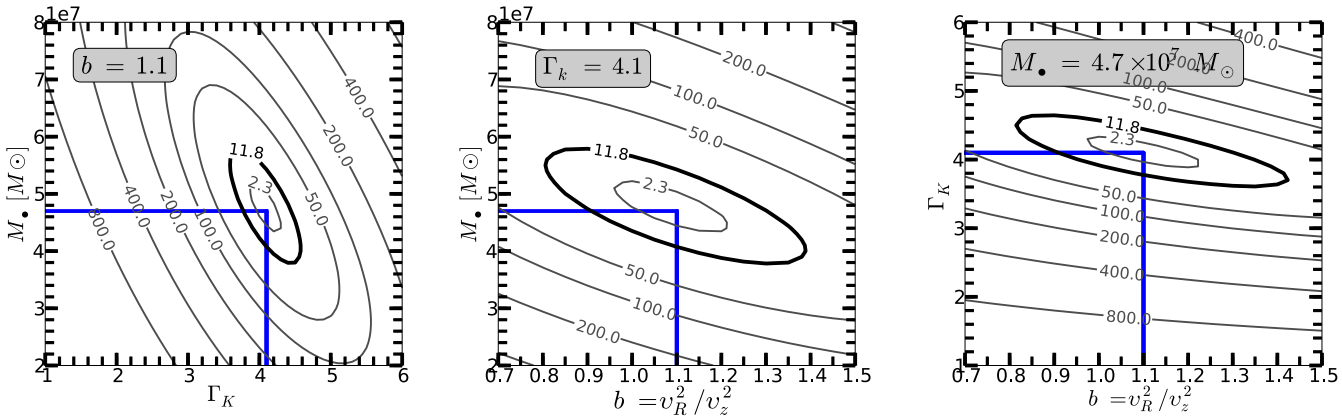

Figure 8. Determination of the best-fitting parameters and the χ^2 minimization for the model C. Left: the plane $M_\bullet \times \Gamma_K$ for b $=$ 1.1 ($\beta_z = 0.09$). Central: the plane $M_\bullet \times b$ for $\Gamma_K = 4.1$. Right: the plane $\Gamma_K \times b$ for $M_\bullet = 4.7 \times 10^7$ M$_\odot$. The values shown at the contours are for the quantity $\Delta\chi^2 = \chi^2 - \chi^2_{\rm min}$ where $\chi^2_{\rm min} = 25.48$. The blue lines indicate the best-fitting parameters in each plane. The two inner contours shown correspond to the values of $\Delta\chi^2 = 2.3$ and $\Delta\chi^2 = 11.8$ that are the boundaries of the 1σ and 3σ confidence regions for the two parameters together (Press et all. 2007).

Table 2. Summary of the models with constant anisotropy.

Model (1)	i (2)	$M_\bullet$ (M$_\odot$) (3)	Γ_K (4)	$b(\beta_z)$ (5)	$\chi^2_{\rm min}$ (6)
A	72°	5.2×10^7	4.3	0.90 (−0.11)	27.21
B	68°	5.0×10^7	4.3	0.95 (−0.05)	26.84
C	64°	4.7×10^7	4.1	1.1 (0.09)	25.48

Note. Column (1): model designation. Column (2): galaxy inclination. Column (3): best-fitting mass of the SMBH. Column (4): best-fitting *K*-band mass-to-light ratio. Column (5): best-fitting anisotropy. Column (6): lowest value of the χ^2 obtained.

In Fig. 9, we present the χ^2 minimization for $M_\bullet$ for models A (black dotted line), B (open circles) and C (green solid line). The values of the parameters Γ_K and b are the best-fitting values of each model. The vertical line indicates the value of the maser determination, $M_{\bullet\,\rm Maser} = 3.82 \times 10^7$ M$_\odot$. The green shaded region corresponds of the $M_\bullet$ values that are within 3σ confidence intervals for the model with $i = 64°$. The best-fitting mass of the SMBH with 3σ of confidence is $M_\bullet = 4.7^{+1.0}_{-0.8} \times 10^7$ M$_\odot$.

4.2.2 *Effects of the PSF in the best-fitting parameters*

One important issue in the dynamical models of galaxies is that before comparing the modelled velocities with the measured ones, we need to convolve the modelled velocities with the PSF of the kinematic observations. For the Jeans anisotropic dynamical models, the convolution is implemented as in appendix of Cappellari (2008). We used a model for the NIFS PSF that is obtained from an MGE fit to the observations of three stars observed in the same night of the galaxy observations, as described in Section A2. As the time needed for the galaxy observations are longer (600 s) than that of the stars observations (15 s), there is the possibility that we are underestimating the NIFS PSF.

In order to verify the influence of a possible broader PSF (larger FWHM) in the modelled kinematics and best-fitting value for $M_\bullet$, we ran again the model C with $\Gamma_K = 4.1$, and $b = 1.10$ and performed the χ^2 minimization for $M_\bullet$. We used two broader PSF models obtained from the model described in Section A2: in the first one, we increase the dispersions (listed in second column of Table A2) of the Gaussians of the MGE model of the PSF by a factor of 1.5 and in the second we duplicated the values of the dispersions of the Gaussians.

In Fig. 10, we present the modifications in the χ^2 minimization and in the best-fitting value of $M_\bullet$ introduced by the increase of the NIFS PSF by a factor of 1.5 (represented by the black dotted line) and by a factor of 2.0 (represented by the open circles). The continuous line is for model C which provides a $\chi^2_{\rm min} = 25.48$ for $M_\bullet = 4.7 \times 10^7$ M$_\odot$. For the model with the PSF 1.5 times broader, we obtained $\chi^2_{\rm min} = 26.17$ for $M_\bullet = 4.9 \times 10^7$ M$_\odot$ which is within

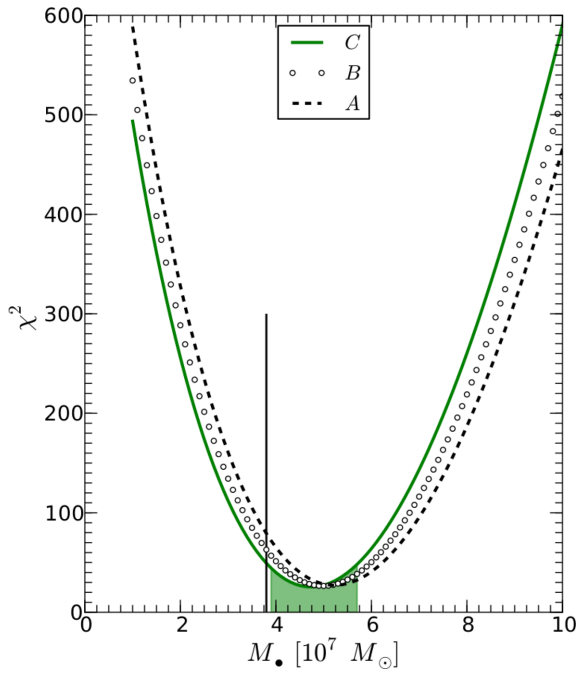

Figure 9. Variation of χ^2 with the SMBH mass for the models with constant anisotropy. The green solid line represents the minimization of χ^2 as a function of $M_\bullet$ for the best-fitting model with $i = 64°$ (Model C). The values of $M_\bullet$ in the shaded region correspond to the 3σ uncertainty in this parameter, thus the best-fitting mass of the SMBH is $M_\bullet = 4.7^{+1.0}_{-0.8} \times 10^7$ M$_\odot$. The open circles represent the minimization for the model with $i = 68°$ (Model B). The black dashed line represents the minimization for the model with $i = 72°$ (Model A). The vertical line indicates the value of the maser determination, $M_{\bullet\,\rm Maser} = 3.82 \times 10^7$ M$_\odot$.

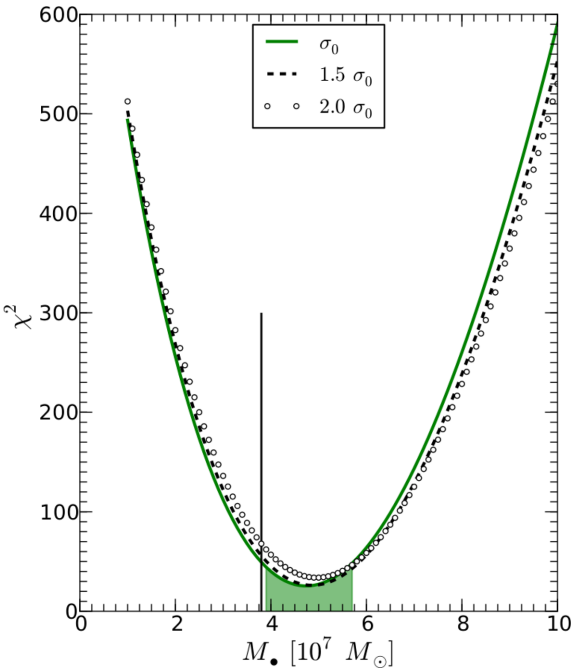

Figure 10. Effects of variations in the PSF width in the best-fitting mass of the SMBH. The green solid line represents the variation of χ^2 with the mass of the SMBH for the model C. The dashed black line shows the variation of χ^2 using a model for the NIFS PSF with a dispersion σ that is 50 per cent larger than that presented in Appendix A2, which results in a $\chi^2_{\rm min} = 26.17$ for $M_\bullet = 4.9 \times 10^7$ M$_\odot$. The open circles shows the variation of χ^2 using a model for the NIFS PSF with a dispersion σ that is 100 per cent larger than the original and results in a $\chi^2_{\rm min} = 33.83$ for $M_\bullet = 5.0 \times 10^7$ M$_\odot$. The shaded region shows the range of values of $M_\bullet$ that are inside the 3 σ uncertainty of the best-fitting value of $M_\bullet$ of the reference model (Model C). The vertical line indicates the value of the maser determination, $M_{\bullet\,\rm Maser} = 3.82 \times 10^7$ M$_\odot$.

the 1σ uncertainties of the best-fitting model. For the model with the PSF two times broader, $\chi^2_{\rm min} = 33.83$ for $M_\bullet = 5.0 \times 10^7$ M$_\odot$. For both cases, the values for the mass of the SMBH that best reproduce the measured kinematics are inside the 3σ confidence interval of the best-fitting model and the modelled velocities still reproduce the observed ones.

4.2.3 Models with variable anisotropy

As the solutions of the Jeans equations are presented for each Gaussian individually and the total second moment is the quadratic sum of the contributions of each Gaussian, it is possible to assign different values of anisotropy for each Gaussian of the MGE model that describes the galaxy luminosity density. As exemplified by Krajnović et al. (2009) for the galaxies NGC 2549 and NGC 524 and by Gebhardt et al. (2003), spatial variations in the velocity anisotropy are frequent. In order to test how better the measured kinematics can be reproduced by models with variable anisotropy, we considered two scenarios. In the first, we assumed that there is a radial variation in the anisotropy. We considered two different values for the anisotropy parameters b_k, one for the four inner Gaussians that have $\sigma_k < 1.0$ arcsec and another value for the remaining outer Gaussians. Then, we performed the χ^2 minimization for two different inclinations $i = 64^\circ$ (model D) and $i = 72^\circ$ (model E). In a second scenario, we assigned one anisotropy value for the Gaussians with axial ratio $q_k < 0.5$ representative of the disc component and another anisotropy value for the Gaussians with axial ratio $q_k \geq 0.5$ representative of the spheroidal component. This minimization was also performed for two values of the galaxy inclination: $i = 64^\circ$ (model F) and $i = 72^\circ$ (model G). For all the models with variable anisotropy, we considered a constant mass-to-light ratio of $\Gamma_k = 4.1$. The best-fitting parameters for the models with variable anisotropy are presented in Table 3. The best-fitting model with $\chi^2_{\rm min} = 25.24$ was obtained for the inclination $i = 64^\circ$ and with a radially variable anisotropy (Model D). The dynamical parameters of this model are $M_\bullet = 4.8 \times 10^7$ M$_\odot$, $\Gamma_K = 4.1$, $b_{\rm in} = 1.10$ and $b_{\rm out} = 1.05$. The average absolute error in the second moment over all pixels of the kinematic field is of 5.8 per cent. The results of the model for the second moment and the comparison with the observed $V_{\rm rms}$ are shown in Fig. 11.

Table 3. Summary of the models with variable anisotropy.

Model (1)	i (2)	$M_\bullet$ (M$_\odot$) (3)	$b_{\rm in}$ (β_z) (4)	$b_{\rm out}$ (β_z) (5)	$\chi^2_{\rm min}$ (6)
D	64°	4.8×10^7	1.10 (0.09)	1.05 (0.05)	25.24
E	72°	5.3×10^7	1.00 (0.00)	0.90 (−0.11)	28.65
			$b_{\rm disc}$ (β_z)	$b_{\rm bulge}$ (β_z)	
F	64°	4.8×10^7	1.25 (0.20)	1.05 (0.05)	25.34
G	72°	5.3×10^7	1.30 (0.23)	0.85 (−0.17)	27.90

Note. Column (1): model designation. Column (2): galaxy inclination. Column (3): best-fitting mass of the SMBH. Column (4): for models (D) and (E) these are these are the values of the anisotropy parameter of the inner four Gaussians, for models (F) and (G) these are the values of the anisotropy parameter of the Gaussians with axial ratio q_k lower than 0.47. Column (5): for models (D) and (E) these are the values of the anisotropy parameter of the outer eight Gaussians, for models (F) and (G) these are the values of the anisotropy parameter of the Gaussians with axial ratio q_k higher than 0.5. Column (6): lowest value of the χ^2 obtained.

The top-left panel presents the observed $V_{\rm rms}$ after bi-symmetrization. The minimum value for $V_{\rm rms}$ is ≈85 km s^{-1} and occurs at the most distant locations from the galaxy centre along the photometric minor axis. The maximum value is ≈180 km s^{-1} at the galaxy centre. The top central panel shows the $\langle v^2_{\rm los}\rangle^{1/2}$ distribution for the best-fitting model (model D), showing very good agreement with the measured $V_{\rm rms}$. The top-right panel shows the residuals $\left(V_{\rm rms} - \langle v^2_{\rm los}\rangle^{1/2}\right)$. The differences between the measured and modelled velocities are small, with the highest positive residual being ≈12 km s^{-1} (which represents an error of ≈11 per cent in relation to the measured velocity in this position), and highest negative residual of ≈−13 km s^{-1} representing an error of ≈12 per cent. The average error over the whole field is ≈3 per cent. The good agreement between the modelled and measured velocities is also clear in the superposition of the isovelocity curves of the model on those of the measured velocity field presented in the top central panel.

In the bottom panels, we present linear cuts across the galaxy centre in three different directions: along the galaxy major axis in the left-hand panel, the minor axis in the central panel and along a diagonal cut in the right-hand panel. The black points show the measured values for $V_{\rm rms}$ with 1σ error bars represented by the shaded region. The red solid lines show our best-fitting model for the projected second moment of the velocity ($\langle v^2_{\rm los}\rangle^{1/2}$). The red dotted lines show the residuals between the observations and the best-fitting model. Along the galaxy major axis, the modelled velocities reproduced very well the observed ones. Along the galaxy minor

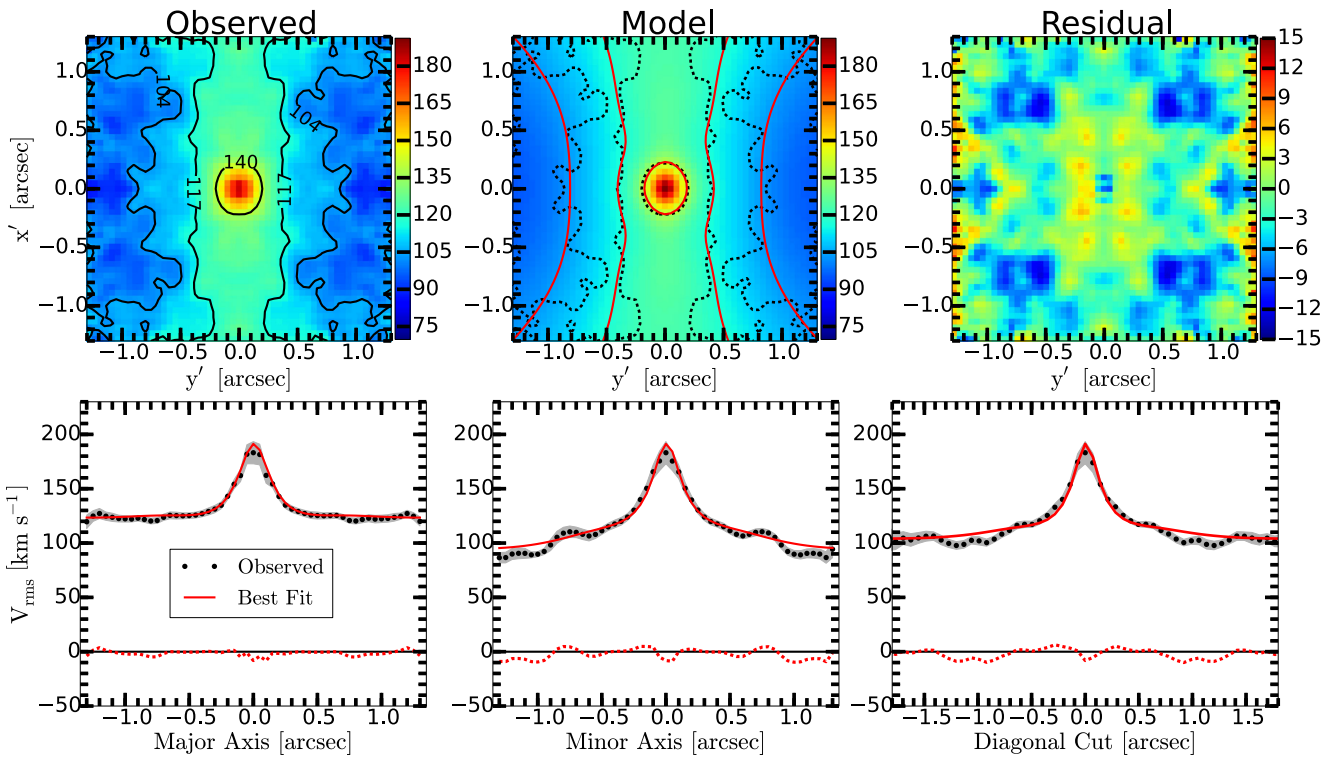

Figure 11. Comparison between the observed $V_{\rm rms}$ and the best-fitting $\langle \upsilon_{\rm los}^2 \rangle^{1/2}$ (Model D). Top left: the observed $V_{\rm rms} = \sqrt{V^2 + \sigma^2}$ after symmetrization; the contours correspond to the isovelocity curves of 104, 117 and 140 $\rm km s^{-1}$. Top central: the best-fitting model presenting the superposition of the isovelocity curves of the modelled (red solid lines) and observed (black dotted lines) velocities. Top right: the residual $V_{\rm rms} - \langle \upsilon_{\rm los}^2 \rangle^{1/2}$ in $\rm km s^{-1}$. Bottom left: linear cuts along the galaxy major axis ($x\prime$), where the black points show the observed symmetrized $V_{\rm rms}$, the red solid lines are the result of our best-fitting model, the shaded bands are the 1σ errors in the velocity measurements. Bottom central and right-hand panels show the same quantities as the left-hand panel along the galaxy minor axis and along the diagonal direction, respectively.

axis, the largest differences occur in the most distant regions from the galaxy centre.

In Fig. 12, we present the χ^2 minimization for $M_\bullet$ for the models D (green solid line) and E (black dashed line). The vertical line indicates the value of the maser determination, $M_{\bullet\,\rm Maser} = 3.82 \times 10^7\,\rm M_\odot$. The green shaded region corresponds to the $M_\bullet$ values that are inside the 3σ confidence interval for the model with $i = 64^\circ$ (Model D). The best-fitting mass of the SMBH with 1σ of confidence is $M_\bullet = 4.8^{+0.8}_{-0.9} \times 10^7\,\rm M_\odot$.

4.2.4 *Comparison with previous results*

We can now compare the value of the SMBH mass that we have obtained with the previous ones from the literature. When compared with the maser determination (Greenhill et al. 1995; Herrnstein et al. 1999) of $M_{\bullet\,\rm Maser} = 3.82 \times 10^7\,\rm M_\odot$ our value of $M_\bullet = 4.8^{+0.8}_{-0.9} \times 10^7\,\rm M_\odot$ is ≈25 per cent larger.

For comparison, the previous stellar dynamical determination obtained via Schwarzschild models from long-slit data by Siopis et al. (2009) ($M_{\bullet\,\rm Schw} = 3.3 \pm 0.2 \times 10^7\,\rm M_\odot$) is 15 per cent lower than the maser value. Making a direct comparison between the two dynamical determinations, there is a difference of ≈45 per cent in the best-fitting values for the mass of the SMBH. The main factors that contribute to this difference are as follows.

(i) As we have shown in Fig. B1 of Appendix B, the measured velocity dispersions of our NIFS data are considerably higher than those tabulated for the STIS data, being the differences larger than the error bars for most of the points analysed. The differences between the values of the $\rm V_{rms}$ are consistent with the differences introduced in the modelled velocity second moment by the difference of the mass of the SMBH from the models.

(ii) Another possible cause for these difference in the mass of the SMBH can be an over-subtraction of the contribution from the AGN to the surface brightness distribution in the NICMOS image. The uncertainties introduced in the model by this factor are discussed in Appendix C.

(iii) A third factor that could cause the difference in the SMBH mass derived using the two methods are the intrinsic differences between the dynamical models used (Schwarzschild versus Jeans models). The adopted JAM method makes more restrictive assumptions than Schwarzschild method. Although the two methods have been shown to generally agree quite well in real galaxies, some differences are not unexpected.

4.2.5 *The velocity first moment*

In order to model the velocity first moment, it is necessary to make extra assumptions in the Jeans equations to specify how the second moment is composed in terms of ordered and random motions. We use the approximation that the tangential component of the velocity first moment of each Gaussian is a function of the difference between the tangential and radial components of the velocity second moment of each Gaussian, $\langle \upsilon_\phi \rangle_k = \kappa_k (\langle \upsilon_\phi^2 \rangle_k - \langle \upsilon_R^2 \rangle_k)^{1/2}$. [See section 3.2.1 of Cappellari (2008) for a more complete explanation].

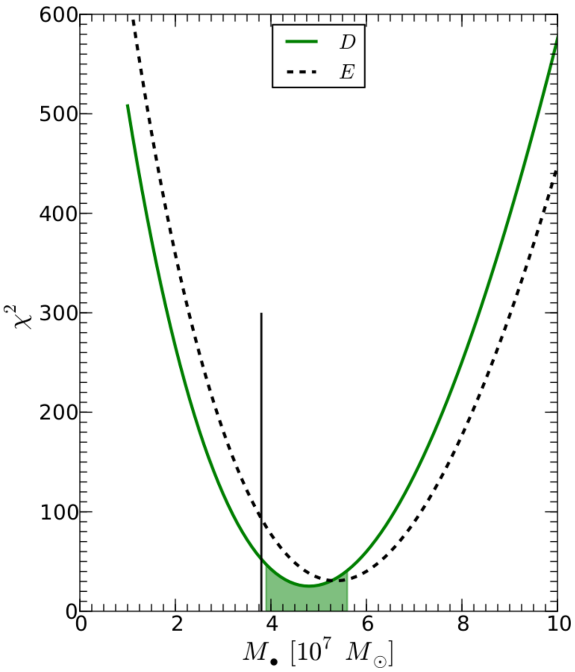

Figure 12. Variation of the χ^2 with the SMBH mass for the models with variable anisotropy. The green solid line represents the minimization of χ^2 as a function of the $M_\bullet$ for the best-fitting model with $i = 64^\circ$ (Model D). The values of $M_\bullet$ in the shaded region corresponds to the 3σ confidence interval for this parameter, thus the best-fitting mass of the SMBH is $M_\bullet = 4.8^{+0.8}_{-0.9} \times 10^7\,\mathrm{M}_\odot$. The black dashed line is the χ^2 minimization for the model with $i = 72^\circ$ (Model E).

Adopting the above assumption, we modelled the velocity first moment using the best-fitting parameters of model E. A comparison between the observed rotation velocity field and the modelled first moment for this model is presented in Fig. 13.

The top-left panel shows the measured velocity field for V. The top central panel shows the modelled velocity first moment $\langle v_{\rm los}\rangle$ with $\kappa_k = 0.92$ and the best-fitting values of model D. The top-right panel shows the residuals. The bottom-right panel shows the residuals in per cent. The bottom-left and central panels compare the measured and modelled velocity fields along the galaxy major axis and along a diagonal cut. It can be observed that the maximum residuals reach about 20 km s^{-1} which correspond to ≈50 per cent, as they are observed in the regions along the minor axis where the velocities are lowest. The residuals are higher than 30 per cent within the inner 0.5 arcsec. In the outer regions, the differences between the model and measurements are lower than 30 per cent. But the bottom panels highlight that the modelled velocity first moment does not reproduce the observed rotation mostly in the region between 0.1 and 0.8 arcsec (3.5 pc and 30 pc).

The discrepancy between the modelled velocity first moment field and the measured centroid velocity field, does not affect our conclusion about the mass of the SMBH, that is mostly based on the fit of the second moment. The first moment derived from the model depends on an extra assumption: that the tangential anisotropy is the same everywhere, what may not be true. A more likely explanation for the discrepancy is however the inaccuracy in the deprojection of the luminous stellar density from the observed surface brightness. The deprojection is known to be mathematically degenerate (Rybicki 1987; Gerhard & Binney 1996), with the effect becoming quite significant at low inclination (Romanowsky & Kochanek

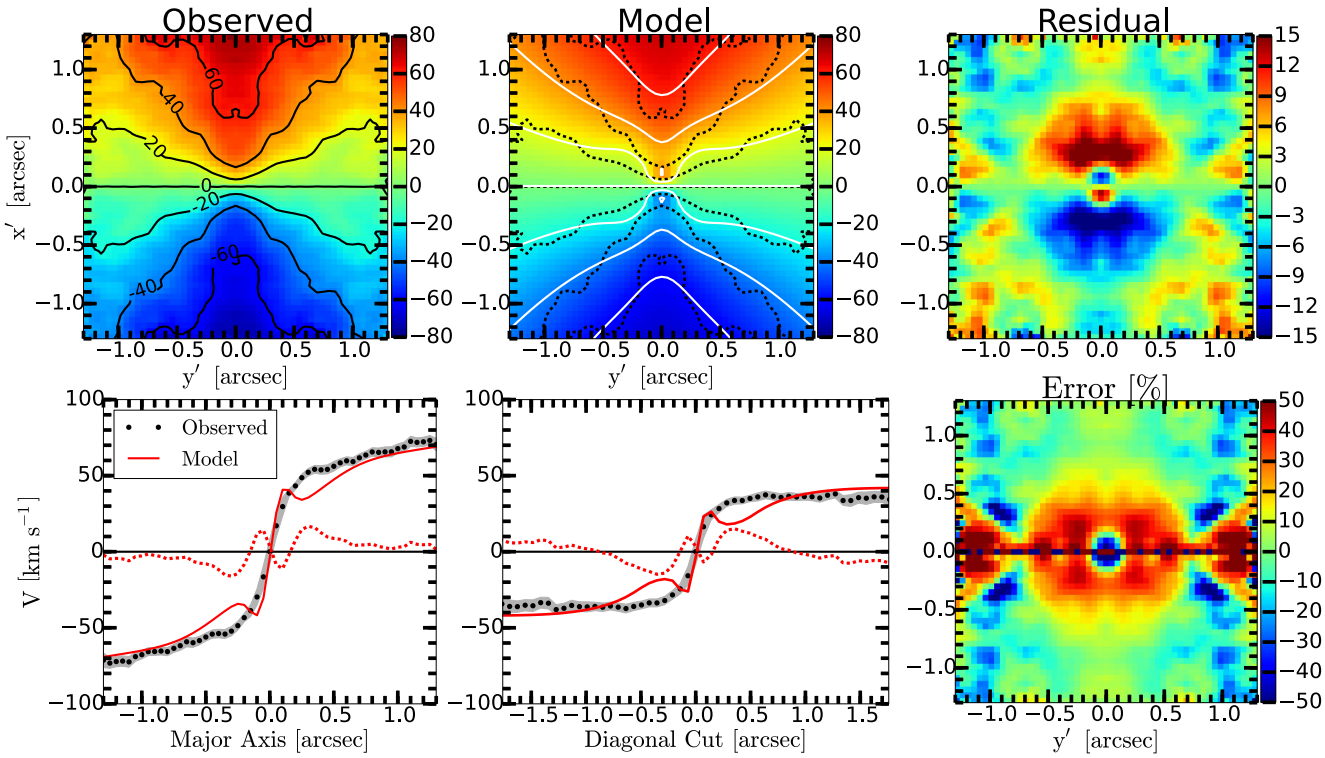

Figure 13. Comparison between the measured centroid velocity V and the first moment $\langle v_{\rm los}\rangle$ for model D. Top left: measured velocity V; the contours are for the isovelocity curves of 0.0, ±20, ±40, ±60 km s^{-1}. Top central: modelled $\langle v_{\rm los}\rangle$ with the best-fitting values of $M_\bullet = 4.8 \times 10^7\,\mathrm{M}_\odot$, $\Gamma_K = 4.1$, $b_{\rm in} = 1.10$ and $b_{\rm out} = 1.05$ obtained from the fit of the second moment and $\kappa = 0.9$. Top right: residuals in km s^{-1}. Bottom right: errors in per cent. Bottom left: linear cuts across the galaxy centre along the galaxy major axis. Bottom central: linear cuts across the galaxy centre in a diagonal direction.

1997). Our galaxy is not seen close to edge-on and could easily hide a weak nuclear disc which would be invisible in the projected photometry, could be showing up in the velocity field, leading to the observed discrepancy between the model and the data. This statement is based on numerical experiments where we tried to force the model to have a flat disc by making the Gaussians of the MGE to have the same axial ratio. Only in this way, one can lower the model inclination and make the inner disc intrinsically very thin within the NIFS FoV. With this forced MGE, one can better reproduce the fast increase in rotation and the difference in V_{rms} between the major and minor axis. Unfortunately, the galaxy overall is not well reproduced by an MGE with constant projected ellipticity. For this reason, our test only shows that the existence of a very thin disc within the NIFS FoV would improve the fit to the kinematics.

5 SUMMARY AND CONCLUSIONS

We have presented a two-dimensional mapping of the stellar kinematics of the inner 3.0×3.0 arcsec^2 ($\sim 100 \times 100$ pc^2) of the galaxy NGC 4258 using NIFS *K*-band data with a signal-to-noise ratio higher than 50 over most of the observed field, spectral resolution of 5300 and spatial resolution of $\approx$4 pc, allowing us to resolve the radius of influence of the SMBH ($\approx$15 pc). The centroid velocity field presents a rotational pattern with a maximum velocity of $\pm 80\,\mathrm{km\,s^{-1}}$, with the SE side approaching and the NW side receding. The stellar velocity dispersion presents an abrupt increase within the inner 0.3 arcsec (10 pc), reaching a value of $180\,\mathrm{km\,s^{-1}}$ at the nucleus, consistent with the presence of an SMBH there.

In order to model the stellar kinematics we built an MGE Jeans Anisotropic Dynamical Model. In this model, the velocity second moment $\langle \upsilon_{los}^2 \rangle^{1/2}$ is a function of three free parameters: the galaxy mass-to-light ratio Γ_K, the anisotropy in the velocity $b = \frac{\overline{\upsilon_R^2}}{\overline{\upsilon_z^2}}$ and the mass of the SMBH $M_\bullet$. We performed a χ^2 minimization in this space of parameters in order to search for the values that best reproduce the measured $V_{rms} = \sqrt{(V^2 + \sigma^2)}$. In order to ensure that all regions of the galaxy, independently of its radial position, have approximately the same relevance in the minimization process we have weighted the χ^2 minimization by assigning errors to the kinematic measurements that are inversely proportional to the galaxy surface brightness at each location. Without this weighting the best-fitting model does not reproduce the measured V_{rms} in the nuclear region of the galaxy and provides a wrong (too high) value for the mass of the SMBH.

We have tried models with only one value for the velocity anisotropy and models with two values. The best-fitting model was obtained adopting a galaxy inclination $i = 64^\circ$ and considering that the galaxy has a radially variable anisotropy in the velocity second moment, being the values of the anisotropy parameter for the inner four Gaussians $b_{in} = 1.10\,(\beta_z = 0.09)$ and for the remaining eight outer Gaussians $b_{out} = 1.05\,(\beta_z = 0.05)$.

Considering the 3σ confidence intervals, we have obtained a mass-to-light ratio of $\Gamma_k = 4.1^{+0.4}_{-0.5}$ and the best-fitting SMBH mass of $M_\bullet = 4.8^{+0.8}_{-0.9} \times 10^7\,\mathrm{M}_\odot$. These 3σ uncertainties of our model are comparable to the typical values for the uncertainties of stellar dynamical models for other galaxies, that usually are lower than 50 per cent for the mass of the SMBH (McConnell et al. 2011). This provides further confirmation of the robustness of the stellar dynamical determinations. It is worth noting that an accurate BH masses was obtained even when using a simple model and only fitting the kinematics within the innermost few arcseconds, without the need for a large-scale model of the galaxy dynamics.

ACKNOWLEDGEMENTS

Based on observations obtained at the Gemini Observatory, which is operated by the Association of Universities for Research in Astronomy, Inc., under a cooperative agreement with the NSF on behalf of the Gemini partnership: the National Science Foundation (United States), the Science and Technology Facilities Council (United Kingdom), the National Research Council (Canada), CONICYT (Chile), the Australian Research Council (Australia), Ministério da Ciência e Tecnologia (Brazil) and SECYT (Argentina). Some of the data presented in this paper were obtained from the Mikulski Archive for Space Telescopes (MAST). STScI is operated by the Association of Universities for Research in Astronomy, Inc., under NASA contract NAS5-26555. Support for MAST for non-HST data is provided by the NASA Office of Space Science via grant NNX13AC07G and by other grants and contracts. This work has been partially supported by the Brazilian institution CNPq. MC acknowledges support from a Royal Society University Research Fellowship. We thank the referee, Remco van den Bosch for the valuable suggestions that helped to improve the paper.

REFERENCES

Binney J., Tremaine S., 2008, Galactic Dynamics, 2nd edn. Princeton Univ. Press, Princeton, NJ
Binney J., Davies R. L., Illingworth G. D., 1990, ApJ, 361, 78
Cappellari M., 2002, MNRAS, 333, 400
Cappellari M., 2008, MNRAS, 390, 71
Cappellari M., Emsellem E., 2004, PASP, 116, 138
Cappellari M., McDermid R. M., 2005, Class. Quantum Gravity, 22, 347
Cappellari M. et al., 2006, MNRAS, 366, 1126
Cappellari M., Neumayer N., Reunanen J., van der Werf P. P., de Zeeuw P. T., Rix H.-W., 2009, MNRAS, 394, 660
Cappellari M. et al., 2010, in Debattista V. P., Popescu C. C., eds, AIP Conf. Proc. Vol. 1240, Hunting for the Dark: the Hidden Side of Galaxy Formation. Am. Inst. Phys., New York, p. 211
Cappellari M. et al., 2012, Nature, 484, 485
Cappellari M. et al., 2013a, MNRAS, 432, 1709
Cappellari M. et al., 2013b, MNRAS, 432, 1862
Cecil G., Wilson A. S., Tully R. B., 1992, ApJ, 390, 365
Cecil G. et al., 2000, ApJ, 536, 675
Chary R., Becklin E. E., Evans A. S., Neugebauer G., Scoville N. Z., Matthews K., Ressler M. E., 2000, ApJ, 531, 756
Cortés J. R., Kenney J. D. P., Hardy E., 2008, ApJ, 683, 78
Cretton N., van den Bosch F. C., 1999, ApJ, 514, 704
de Zeeuw P. T. et al., 2002, MNRAS, 329, 513
Emsellem E., 2013, MNRAS, 433, 1862
Emsellem E., Monnet G., Bacon R., 1994, A&A, 285, 723
Feldmeier A. et al., 2013, A&A, 554, A63
Gebhardt K. et al., 2003, ApJ, 583, 92
Gerhard O. E., Binney J. J., 1996, MNRAS, 279, 993
Greenhill L. J., Jiang D. R., Moran J. M., Reid M. J., Lo K. Y., Claussen M. J., 1995, ApJ, 440, 419
Herrnstein J. R. et al., 1999, Nature, 400, 539
Herrnstein J. R., Moran J. M., Greenhill L. J., Trotter A. S., 2005, ApJ, 629, 719
Jarrett T. H., Chester T., Cutri R., Schneider S. E., Huchra J. P., 2003, AJ, 125, 525
Jeans J. H., 1922, MNRAS, 82, 122
Joseph C. L. et al., 2001, ApJ, 550, 668
Krajnović D., McDermid R. M., Cappellari M., Davies R. L., 2009, MNRAS, 399, 1839

Krist J., Hook R., Stoehr F., 2010, Astrophysics Source Code Library, record ascl:1010.057
Lablanche P. Y. et al., 2012, MNRAS, 424, 1495
Lützgendorf N., Kissler-Patig M., Noyola E., Jalali B., de Zeeuw P. T., Gebhardt K., Baumgardt H., 2011, A&A, 533, A36
Lützgendorf N., Kissler-Patig M., Gebhardt K., Baumgardt H., Noyola E., Jalali B., de Zeeuw P. T., Neumayer N., 2012, A&A, 542, A129
Lützgendorf N. et al., 2013, A&A, 552, A49
McConnell N. J., Ma C.-P., Gebhardt K., Lauer Tod R., Graham James R., 2011, Nature, 480, 215
McGregor P. J. et al., 2003, in Masanori I., Moorwood A. F. M., eds, Proc. SPIE Conf. Ser. Vol. 4841, Instrument Design and Performance for Optical/Infrared Ground-based Telescopes. SPIE, Bellingham, p. 1581
Magorrian J. et al., 1998, AJ, 115, 2285
Medling A. M., Ammons S. M., Max C. E., Davies R. I., Engel H., Canalizo G., 2011, ApJ, 743, 32
Miyoshi M., Moran J., Herrnstein J., Greenhill L., Nakai N., Diamond P., Inoue M., 1995, Nature, 373, 127
Nagai R., Miyamoto M., 1976, PASJ, 28, 1
Neumayer N., Walcher C. J., 2012, Adv. Astron., 2012
Pastorini G. et al., 2007, A&A, 469, 405
Press W. H., Teukolsky S. A., Vetterling W. T., Flannery B. P., 2007, Numerical Recipes: The Art of Scientific Computing, 3rd edn. Cambridge Univ. Press, New York
Raimundo S. I., Davies R. I., Gandhi P., Fabian A. C., Canning R. E. A., Ivanov V. D., 2013, MNRAS, 431, 2294
Riciputi A., Lanzoni B., Bonoli S., Ciotti L., 2005, A&A, 443, 133
Romanowsky A. J., Kochanek C. S., 1997, MNRAS, 287, 35
Rybicki G. B., 1987, in de Zeeuw P. T., ed., Proc. IAU Symp. Vol. 127, Structure and Dynamics of Elliptical Galaxies, Reidel, Dordrecht, p. 397
Satoh C., 1980, PASJ, 32, 41
Sawada-Satoh S., Ho P. T. P., Muller S., Matsushita S., Lim J., 2007, ApJ, 658, 851
Schwarzschild M., 1979, ApJ, 232, 236
Scoville N., 1997, HST Proposal, 7230
Seth A. et al., 2010, in Debattista V. P., Popescu C. C., eds, AIP Conf. Proc. Vol. 1240, Hunting for the Dark: the Hidden Side of Galaxy Formation. Am. Inst. Phys., New York, p. 227
Seth A. C. et al., 2014, Nature, 513, 398
Siopis C. et al., 2009, ApJ, 693, 946
Statler T. S., Dejonghe H., Smecker-Hane T., 1999, AJ, 117, 126
Tremaine S., Richstone D. O., Byun Y.-I., Dressler A., Faber S. M., Grillmair C., Kormendy J., Lauer T. R., 1994, AJ, 107, 634
van Albada G. D., 1980, A&A, 90, 123
van Albada T. S., Bertin G., Stiavelli M., 1995, MNRAS, 276, 1255
van der Kruit P. C., 1974, ApJ, 192, 1
van der Marel R. P., 1991, MNRAS, 253, 710
van der Marel R. P., Binney J., Davies R. L., 1990, MNRAS, 245, 582
van der Marel R. P., Cretton N., de Zeeuw P. T., Rix H.-W., 1998, ApJ, 493, 613
Verolme E. K. et al., 2002, MNRAS, 335, 517
Wilkes B. J., Schmidt G. D., Smith P. S., Mathur S., McLeod K. K., 1995, ApJ, 455, L13
Wilson A. S., Yang Y., Cecil G., 2001, ApJ, 560, 689
Winge C., Riffel R. A., Storchi-Bergmann T., 2009, ApJS, 185, 186
Yang Y., Li B., Wilson A. S., Reynolds C. S., 2007, ApJ, 660, 1106
Yuan F., Markoff S., Falcke H., Biermann P. L., 2002, A&A, 391, 139

APPENDIX A: MGE PARAMETERS FOR THE NICMOS AND NIFS PSF

In this appendix, we present the MGE models for the NICMOS and NIFS PSF's and the agreement of the MGE model of the NICMOS PSF with those of the TINYTIM model.

A1 The NICMOS PSF

We modelled the NICMOS PSF by a set of four approximately circular Gaussians using the MGE method. The resulting Gaussian parameters are presented in Table A1. In Fig. A1, we present the comparison between the luminosity profiles of the TINYTIM PSF showed by the black open circles and our MGE modelled PSF showed by the blue solid line.

In order to verify the effects of the small differences between the MGE model and the real PSF in the convolution procedure, we present in Fig. A2 a comparison of the convolution of the surface brightness distribution of NGC 4252 presented in Section 4.1 with the TINYTIM PSF (black open circles) and with our MGE model for the NICMOS PSF (red solid line) for the central 6.0 arcsec of the galaxy. The left-hand panel shows a linear cut across the galaxy centre and along the photometric major axis and the right-hand panel along the galaxy minor axis. In both directions, the differences are very small in most of the regions.

Table A1. Gaussian parameters of the MGE model for the NICMOS PSF.

Σ'_k(Total Counts)	σ'_k (arcsec)	q'_k
0.52	0.084	≈1.0
0.34	0.242	≈1.0
0.06	0.789	≈1.0
0.08	2.671	≈1.0

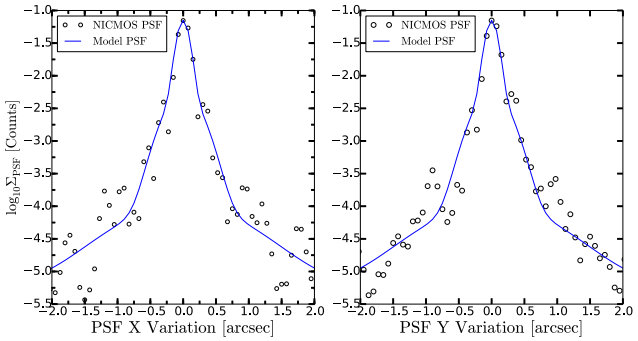

Figure A1. NICMOS PSF fit. Left: linear cut along the detector horizontal direction showing the radial profile of the NICMOS PSF of the TINYTIM model (black open circles) and of the resulting MGE model for the PSF (blue solid line). Right: same as the left but for the detector vertical direction.

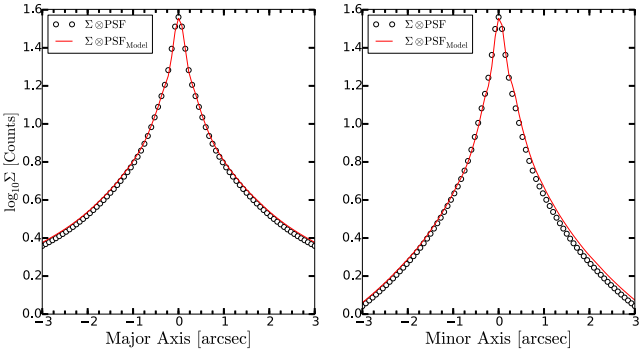

Figure A2. Comparison of the convolution of the MGE model for the surface brightness distribution with the TINYTIM PSF and with the MGE model for the PSF. Left: cuts along galaxy major axis. Right: cuts along galaxy minor axis.

Table A2. Gaussian parameters of the MGE model for the NIFS PSF.

Σ'_k(Total Counts)	σ'_k (arcsec)	q'_k
0.29	0.045	≈1.0
0.20	0.069	≈1.0
0.15	0.103	≈1.0
0.27	0.317	≈1.0
0.09	0.543	≈1.0

A2 The NIFS PSF

The MGE model of the NIFS PSF is performed using the average image of three reconstructed images from the data cubes of three stars observed with NIFS in the same night of the observations of the galaxy. The Gaussian parameters of the MGE model for the NIFS PSF are presented in Table A2. In Fig. A3, we present a comparison between the resulting MGE model and the NIFS PSF. In the left-hand panel, we show a linear cut along the detector horizontal axis of the NIFS PSF (black open circles) and of the MGE model (blue solid line). In the right-hand panel, we show a linear cut along the detector vertical axis.

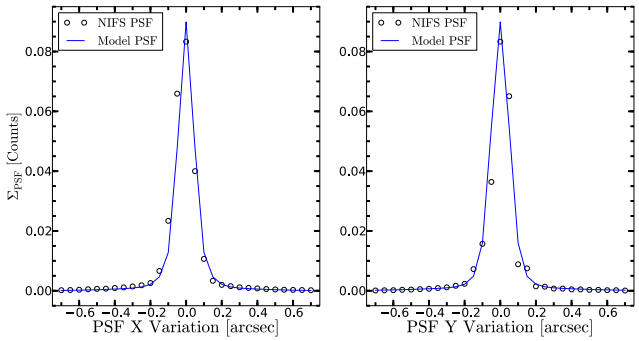

Figure A3. NIFS PSF fit. Left: linear cut along the detector horizontal direction showing the radial profile of the NIFS PSF obtained from observations of three stars (black open circles) and of the resulting MGE model for the PSF (blue solid line). Right: same as the left but for the detector vertical direction.

APPENDIX B: COMPARISON BETWEEN THE KINEMATICS MEASUREMENTS OF NIFS AND STIS

In this section, we present a comparison between the measured velocities and velocity dispersions of our NIFS data and the previous published long-slit data from the *HST*/STIS instrument used by Siopis et al. (2009) to determine the mass of the SMBH in the nucleus of NGC 4258 through Schwarzschild dynamical orbit superposition. In Table B1, we present kinematic measurements with 1σ errors from the STIS data (Siopis et al. 2009) for the positions along the galaxy major axis coincident with our NIFS measurements. In column 1, we list the positions of the extractions; in column 2, the values of the centroid velocities obtained from the STIS data; in column 3, the values of the centroid velocities from the NIFS data; in columns 4 and 5, we present the values of the velocity dispersion measurements from the STIS and NIFS data, respectively.

The differences between the measured velocities from both instruments are shown in Fig. B1. The top panel shows the centroid velocities: the blue diamonds are the NIFS data with the 1σ errors being represent by the shaded grey band, the open circles with the error bars are the STIS data. In the region inside 0.2 arcsec, the STIS data show a steeper velocity curve than the NIFS data, while for the outer region the error bars overlap. We attribute this difference to the somewhat better angular resolution of the STIS when compared to that of NIFS.

The middle panel shows the velocity dispersions: the NIFS data have σ values ≈20 km s^{-1} higher than those from the STIS data. We attribute this difference to the smaller FWHM of the STIS PSF and to the different methods and templates used for the σ determinations: while we have used the stellar templates library of Winge et al. (2009), Siopis et al. (2009) used only one stellar template (HR 7615).

In the bottom panel, we show the resulting $V_{\rm rms}$ compared to different models. The black dashed line is the velocity second moment along the galaxy major axis from our best-fitting model with the parameters $b_{\rm in} = 1.10\,(\beta_z = 0.09)$, $b_{\rm out} = 1.05\,(\beta_z = 0.05)$, $\Gamma_K = 4.1$ and $M_\bullet = 4.8 \times 10^7\,{\rm M}_\odot$; the black continuous line is the second moment from a model with the same anisotropy and mass-to-light ratio of the best-fitting model but using the value of $M_{\bullet\,\rm Maser} = 3.82 \times 10^7\,{\rm M}_\odot$; and the red dash–dotted line is a model using the value of $M_{\bullet\,\rm Schw} = 3.3 \times 10^7\,{\rm M}_\odot$. While our best-fitting model

Table B1. Comparison between NIFS and STIS kinematic measurements along the galaxy major axis.

x' (arcsec)	$V_{\rm STIS}$ (km s^{-1})	$V_{\rm NIFS}$ (km s^{-1})	$\sigma_{\rm STIS}$ (km s^{-1})	$\sigma_{\rm NIFS}$ (km s^{-1})
0.00	20 ± 14	0 ± 8	159 ± 17	183 ± 10
0.05	42 ± 6	17 ± 8	142 ± 8	170 ± 10
0.10	60 ± 4	31 ± 6	133 ± 5	155 ± 7
0.17	59 ± 4	40 ± 3	122 ± 5	152 ± 3
0.30	56 ± 6	51 ± 2	112 ± 7	120 ± 3
0.50	57 ± 7	55 ± 3	85 ± 6	115 ± 3
0.80	53 ± 8	62 ± 3	96 ± 10	104 ± 3

Note: Column 1 are the positions of the extractions along the galaxy major axis; Column 2 are the centroid velocities from STIS observations as tabulate in table 3 of Siopis et al. (2009); Column 3 are the centroid velocities from the NIFS observations; Column 4 are the velocity dispersions from the STIS observations; Column 5 are the velocity dispersions from the NIFS observations.

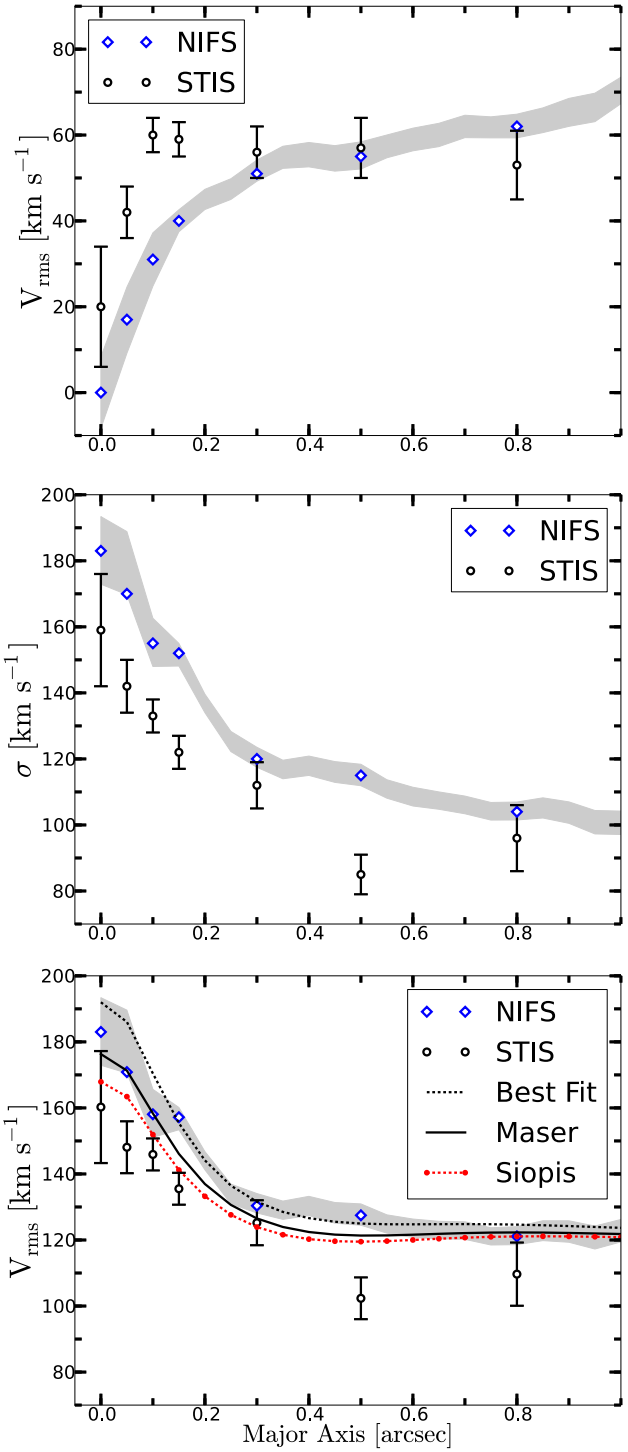

Figure B1. Comparison between STIS and NIFS kinematics along the galaxy major axis. Top: the blue diamonds are the measures of the centroid velocities from our NIFS data with the 1σ error bar represented by the shaded region, the black circles with error bars are the measurements from STIS observations. Middle: velocity dispersions from the NIFS and STIS observations. Bottom: the blue diamonds and black circles are the NIFS and STIS measured $V_{\rm rms}$, respectively. The dashed line is our best-fitting model for the velocity second moment, the continuous line is the modelled velocity second moment using the mass of the SMBH from the maser determination and the dash–dotted line is the model using the mass of the SMBH from Siopis et al. (2009).

gives a $M_\bullet$ somewhat larger than that of the maser determination, the Siopis et al. (2009) gives a $M_\bullet$ somewhat smaller, but the NIFS measurements gives $V_{\rm rms}$ values closer to the one from the model with $M_\bullet = M_{\bullet\,\rm Maser}$.

APPENDIX C: SUBTRACTION OF THE POINT SOURCE

In Section 2.1, we have determined that the luminosity of the AGN contributes with approximately 70 per cent to the total intensity of the central pixel of the NICMOS image. Thus, the total luminosity subtracted from the galaxy image in order to eliminate the contribution of the AGN is of the order of $\approx 1.9 \times 10^7\,{\rm L}_{\odot K}$. Using the mass-to-light ratio of $\Gamma_k = 4.1$ as obtained from our best-fitting model, this corresponds to a mass of $\approx 7.8 \times 10^7\,{\rm M}_\odot$. In order of investigate how a possible over- or undersubtraction of the AGN contribution affects the determination of the mass of the SMBH, we performed two simplified tests.

In the first test, we assume that only the innermost Gaussian component of the MGE model is affected by the subtraction of the point source. This is a plausible assumption as all the other Gaussians components of the model extend beyond the first Airy ring of the PSF and after the convolution of the surface brightness distribution with the PSF the Gaussian components become even flatter. We then added and subtracted $\approx 0.27 \times 10^7\,{\rm L}_{\odot K}$ (or $\approx 1.12 \times 10^7\,{\rm M}_\odot$) from the innermost Gaussian. In practice, this is equivalent to instead of subtracting 70 per cent of the intensity of the central pixel to subtract 60 and 80 per cent, respectively. The effects on the modelled velocity second moment for the three different subtractions of the AGN contribution are shown in Fig. C1, that presents cuts along the galaxy major and minor axis showing the variation of the modelled velocity second moments. The continuous line is our original best-fitting model (Model D), the dashed line is a model with the same dynamical parameters of the best-fitting model but with an additional mass of $\approx 1.12 \times 10^7\,{\rm M}_\odot$ to the central Gaussian, and the shaded band is the 1σ confidence region for the kinematic measurements. The black filled circles are the model where we subtracted the same mass from the innermost Gaussian. The resulting variation in the velocity second moment of the central pixel of the galaxy for this variation in the mass is of the order of $\pm 12\,{\rm km\,s^{-1}}$.

In the second test, we assumed that the innermost Gaussian has a luminosity of $\approx 0.27 \times 10^7\,{\rm L}_{\odot K}$ higher, (this corresponds to subtract only 60 per cent from the intensity of central pixel, this test is motivated by the fact that this amount of light corresponds approximately to a stellar mass that is equal to the difference in the values for the mass of the SMBH obtained from our best-fitting model and the value from the maser determination) and we use the parameters of anisotropy and mass-to-light ratio of our best-fitting models to investigate how well the three different determinations for the mass of the SMBH (Maser, STIS, ours) reproduce the observed kinematics. The resulting modelled velocity second moments along the galaxy major and minor axes are presented respectively in the left-hand and right-hand panels of Fig. C2. The continuous line corresponds to our best-fitting model, the dashed line is the model using the value for the mass of the SMBH from the maser determination and the black filled circles are the model with the value for the mass of the SMBH determined by Siopis et al. (2009). The shaded band is the 1σ confidence region for the kinematic measurements. Under

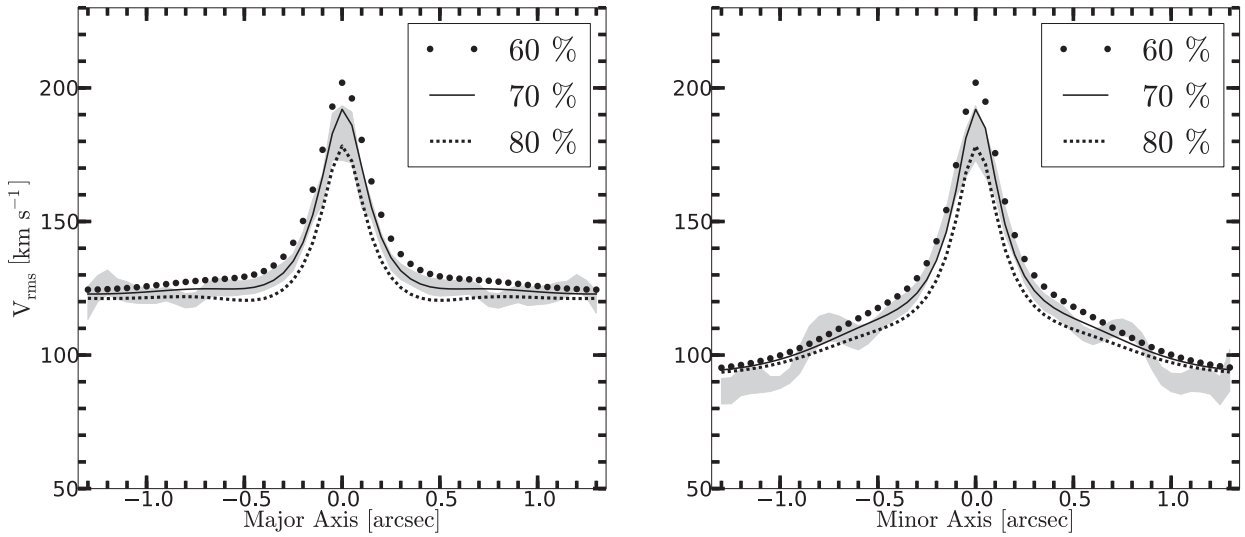

Figure C1. Effects of the point source subtraction on the modelled second moment – Test 1. Left-hand panel: the continuous line is a cut along the galaxy major axis of our best-fitting model, the dotted line shows the modelled second moment using the same dynamical parameters of our best-fitting model and subtracting 10 per cent ($\approx 0.27 \times 10^7$ L$_\odot$) more luminosity in the AGN contribution. The black filled circles represent the resulting model subtracting 10 per cent less luminosity in the AGN subtraction. In the two cases, the luminosity is subtract from the innermost Gaussian of the MGE model. The shaded band are the 1σ confidence intervals for the V_{rms}. Right-hand panel: same as the left-hand panel but for the galaxy minor axis.

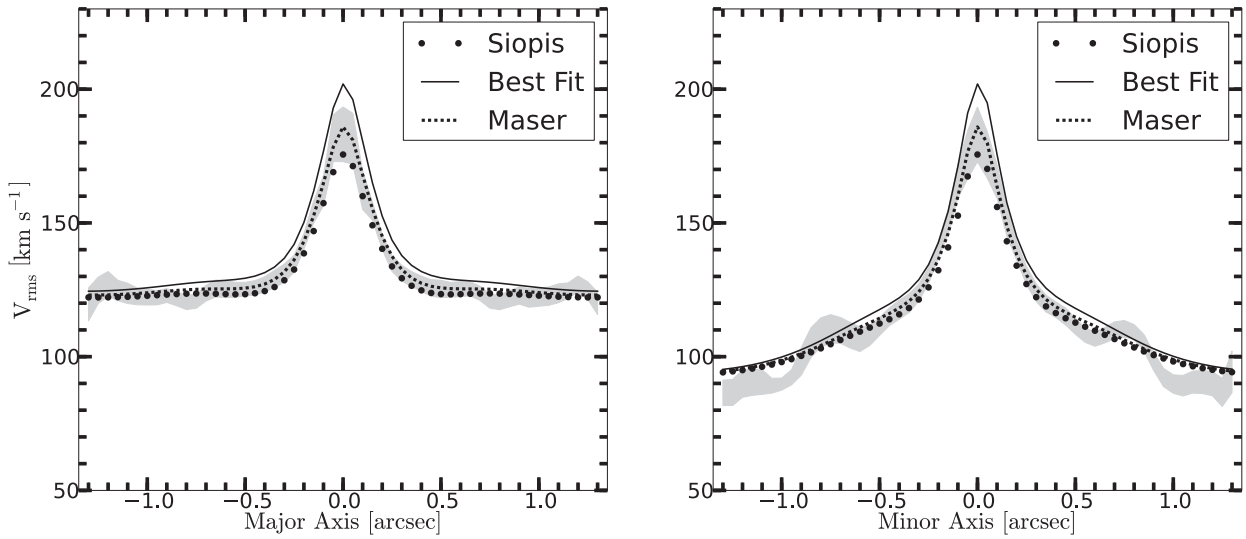

Figure C2. Effects of the point source subtraction on the modelled second moment – Test 2. Left: the continuous line is a cut along the galaxy major axis showing the values of the velocity second moment for the parameters of our best-fitting model and subtracting 10 per cent less luminosity ($\approx 0.27 \times 10^7$ L$_\odot$) in the AGN contribution, The dotted line corresponds to the model using the value of the mass of the SMBH of the maser determination (3.82×10^7 M$_\odot$) and the black bullets is the model using the value of the mass of the SMBH from the previous stellar dynamical determination of Siopis et al. (2009, 3.3×10^7 M$_\odot$).The shaded band are the 1σ confidence intervals for the V_{rms}.

these assumptions, the best fit is obtained for the model with $M_{\bullet\,\mathrm{Maser}} = 3.82 \times 10^7$ M$_\odot$. The model using a mass of $M_{\bullet\,\mathrm{STIS}} = 3.3 \times 10^7$ M$_\odot$ for the SMBH shows a poor but a similar fit to the data to that of our model only that our model are close to the upper envelope of the 1σ band while the of Siopis et al. (2009) are close to the lower envelope.

But we would to point out that the uncertainty in the determination of the AGN is smaller than 10 per cent. Actually, even an oversubtraction of $\approx$5 per cent already leaves a signature on the NICMOS PSF in the image. Our choice of $\approx$5 per cent is because it corresponds in mass to the difference between the value of the SMBH mass of our best-fitting model and that of the maser determination.

SUPPORTING INFORMATION

Additional Supporting Information may be found in the online version of this article:

kinematics.txt (http://mnras.oxfordjournals.org/lookup/suppl/doi:10.1093/mnras/stv536/-/DC1).

Please note: Oxford University Press is not responsible for the content or functionality of any supporting materials supplied by the authors. Any queries (other than missing material) should be directed to the corresponding author for the paper.

This paper has been typeset from a TEX/LATEX file prepared by the author.